kuze.akihiko@jaxa.jp Draft

Draft paper for RSE Special Issue on "Remote sensing of greenhouse gas emissions"

(https://www.journals.elsevier.com/remote-sensing-of-environment/call-for-papers/mapping-greenhouse-gas)

Examining partial-column density retrieval of lower-tropospheric CO_2 from GOSAT target observations over global megacities

A. Kuze[1], Y. Nakamura[2], T. Oda[3], J. Yoshida[2], N. Kikuchi[1], F. Kataoka[4], H. Suto[1], K. Shiomi[1]*

1. Japan Aerospace Exploration Agency, Tsukuba-city, Ibaraki, Japan.

2. NEC Corporation, Fuchu-city, Tokyo, Japan

3. Universities Space Research Association, Columbia, MD, USA.

4. Remote Sensing Technology Center of Japan.

**) Corresponding author: Akihiko Kuze, Japan Aerospace Exploration Agency*

2-1-1 Sengen, Tsukuba-city, Ibaraki, 305-8505, Japan TEL:+81-70-3117-4768

E-mail: kuze.akihiko@jaxa.jp

Abstract

We retrieved and examined the partial-column densities of carbon dioxide (CO_2) in the lower (LT, typically 0–4 km) and upper (UT, typically 4–12 km) troposphere (XCO_2^{LT} and XCO_2^{UT}) collected over six global megacities: Beijing, New Delhi, New York City, Riyadh, Shanghai, and Tokyo. The radiance spectra were collected using the Thermal And Near-infrared Sensor for carbon Observation Fourier-Transform Spectrometer (TANSO-FTS) onboard the Greenhouse gases Observing SATellite (GOSAT). Our retrieval method uniquely utilizes reflected sunlight with two orthogonal components of polarization and thermal emissions. We defined megacity concentration enhancement due to surface CO_2 emissions as XCO_2^{LT} minus XCO_2^{UT}, allowing us to overcome some of the challenges in the enhancement analysis using existing column density data. We examined the relationship between the

XCO_2^{LT} enhancements from the time series of intensive target observations over megacities and the inverse of simulated wind speed, which could be potentially used to estimate surface emissions. Next, we attempted to estimate the average emission intensity for each city from the linear regression slope. We also compared our obtained emission estimates with the Open-Data Inventory for Anthropogenic CO_2 (ODIAC) inventory for evaluation. Our results demonstrate the potential utility of the new partial-column density retrievals for estimating megacity CO_2 emissions. More frequent and comprehensive coverage characterizing the spatial distribution of emissions is necessary to reduce random error and bias associated with the obtained estimate.

Keywords: GOSAT, partial-column density, carbon dioxide, megacity, ODIAC

Highlights of the manuscript (5 items):

- CO_2 density of the lower troposphere using reflected sunlight and thermal emission
- GOSAT megacity data collection using the target mode with revised spatial pattern
- Enhancements calculated by differencing lower and upper partial-column densities
- Emission estimation from the relationship between CO_2 enhancement and wind speed
- Reasonable agreement of obtained emission estimates with an emission inventory

1. Introduction

1.1 Contribution of greenhouse gas (GHG) satellites to climate monitoring under the Paris Climate Agreement

The Paris Agreement was adopted at the 21st session of the Conference of the Parties (COP21) in 2015 (https://unfccc.int/process-and-meetings/the-paris-agreement/the-paris-agreement). It requires countries to submit their climate action plans, namely emission reduction targets known as Nationally Determined Contributions (NDCs), to the United Nations Framework Convention on Climate Change

(UNFCCC). The global progress of NDCs will be evaluated quinquennially based on national measures to achieve the global temperature goal by the mid-21st century. The scientific community has been exploring the use of atmospheric observations to contribute to the successful implementation of the UNFCCC (e.g., Pacala et al., 2010; Jacob et al., 2016; Pinty et al., 2017). Global Earth observations provided by satellites have played a key role in monitoring the status and progress of international compliance with emission reduction agreements, such as the Montreal Protocol (UNEP 2020). The global stocktake in 2023 (GST 2023) (https://unfccc.int/topics/science/workstreams/global-stocktake-referred-to-in-article-14-of-the-paris-agreement) is expected to be the first opportunity to demonstrate the utility of carbon observation satellites in monitoring global compliance with GHG emission reductions. Monitoring significant emission sources from space provides information that contributes to this reduction.

Cities are responsible for more than 70% of global GHG emissions (UN-Habitat, 2012). Over the past decade, the scientific community has expanded its observational capability of cities by using various ground-based observation platforms (Davis et al., 2017; Verhulst et al., 2017; Xueref-Remy et al., 2018; Sargent et al., 2018; Mueller et al., 2018), aircraft (Mays et al., 2009; Brioude et al., 2013; Ahn et al., 2020; Ren et al., 2018; Umezawa et al., 2020), and satellites (Kuze et al., 2009; Crisp et al., 2004; Kiel et al., 2021). Notably, the availability of space-based observations of GHG has enabled the examination of GHG emission information from cities and estimate of their emissions where possible (e.g., Kort et al. 2012, Janardanan et al., 2016; Schwandner et al., 2017; Wu et al., 2018; 2020, Ye et al., 2020; Yang et al., 2020).

1.2 Anthropogenic emission estimations obtained using satellite data

Remote sensing by satellites captures an entire emission plume vertically and horizontally from the top of the atmosphere. Japan’s Greenhouse gas Observing SATellite (GOSAT), launched in 2009, is the first satellite dedicated to measuring GHGs (Kuze et al., 2009). The Thermal And Near-infrared Sensor for carbon Observation Fourier-Transform Spectrometer (TANSO-FTS) onboard GOSAT observes reflected sunlight with two orthogonal components of polarization and thermal emissions simultaneously. GHG data obtained from GOSAT have provided an increased number of scientific and research opportunities to develop, improve, and enhance the ability to retrieve and analyze high-quality GHG data. The collected GHG data and analyses can provide valuable insights to advance carbon cycle science at different scientific and policy-relevant scales (e.g., Ganshin et al., 2012; Kort et al., 2012; Oda et al., 2013; Turner et al., 2015; Janardanan et al., 2016; Ganesan et al., 2017; Varon et al., 2018; Maksyutov et al., 2021). Significantly, the pointing capability of GOSAT has enabled GHG data collection over sizable intense point sources worldwide, such as cities and power plants and examinations of their emission information. Kort et al. (2012) first observed carbon dioxide (CO_2) domes over megacities, such as Los Angeles and Mumbai. Several modeling studies, such as those by Turner et al. (2015) and Janardanan et al. (2016), have also demonstrated the potential utilities of GOSAT observations for detecting potential biases in inventory-based emission estimates. Combining the observations with data from other platforms, Ganesan et al. (2017) demonstrated the feasibility of the objective evaluation of national reported emissions, as stated in the recent refinement of the revised IPCC guidelines (IPCC, 2019; Matsunaga and Maksyutov, 2018). Japan launched its second GHG satellite, GOSAT-2 (2018-), which observes carbon monoxide (CO), CO_2, and methane (CH_4) (Suto et al., 2021). There is a plan to launch a third GHG satellite, the Global Observing SATellite for Greenhous gases and Water cycle (GOSAT-GW) (Hirabayashi, 2020). It is intended as Japan's contribution to global efforts to achieve the Paris Climate Agreement goals. The GOSAT mission's global observations of CO_2 and CH_4 are ongoing and provide the world's longest CO_2 and CH_4 time series from a single satellite (2009-present). It is expected to play a vital role in the emission and climate monitoring activities, such as the upcoming GST, with other satellites under the Committee of Earth Observation Satellites Atmospheric Composition Virtual Constellation (CEOS-AC-VC) (Crisp et al., 2018).

Space-based GHG observing spectrometers launched more recently than those as mentioned above are, for example, NASA's Orbital Carbon Observatory (OCO)-2 and OCO-3 onboard the International Space Station, have provided opportunities to examine the use of satellite data for city emission estimation (Crisp et al., 2004; Eldering et al., 2019; Kiel et al., 2021). Notably, studies based on the OCO-2 and OCO-3 data have illustrated unique challenges. As discussed in Pacala et al. (2010), the size of the GOSAT' footprint (10.5 km in diameter) is larger than that of the OCO-2 instrument (1.

29×2.25 km^2), which may limit its ability to observe relatively weaker CO_2 enhancements due to local sources, such as mid-sized power plants. In addition, the large footprint and severe geophysical difficulties (e.g., clouds and aerosols) have reduced the data yield to a value lower than that required for robust emission estimations (Suto et al., 2021). Sparse pointwise observation patterns have allowed the collection of useful data for large-scale flux inversions, although interpolating data is necessary to capture potential emission plumes from city areas or significant point sources, as compared with spatially denser OCO-2 data (e.g., Schwandner et al., 2017; Nassar et al., 2017; Reuter et al., 2019). Some of these difficulties have been mitigated by the intelligent pointing of GOSAT-2 and will be overcome on future missions, such as GOSAT-GW and ESA's CO_2 monitoring mission (CO2M) (Sierk et al., 2019). However, challenges, such as determining background and boundary inflow (Schuh et al., 2021), potential local vegetation impact (Miller et al., 2020), and consequently estimating local enhancement, are shared by current space-based approaches and thus need to be considered.

1.3 Objectives of this study

Previous studies on megacity observations using GOSAT data, such as Kort et al.(2012), presented enhancement by differentiating GOSAT data obtained in source areas (e.g., cities) from the surrounding areas. From the early years of the GOSAT observations until 2015, the spatial pattern of sampling was relatively sparse, and the number of clear-sky data was limited to estimating emissions (Kuze et al., 2016). This study presents the first partial-column density retrievals obtained for six megacities. We estimated average emissions from satellite observations and wind speed simulations, assuming CO_2 remains locally at the boundary layer during winter months. Retrieving the CO_2 density of the lower troposphere (LT) improves the detectability and removes the inflow into the upper troposphere (UT). Satellites offer another advantage of obtaining frequent and long-term global observations, although single soundings have a more considerable uncertainty (typically 2 ppm or better) than ground and in situ observations. Kuze et al. (2020) first applied the partial-column products to detect a CH_4 at Aliso Canyon in Southern California. After filtering by using wind direction simulation data, the time series data of the TANSO-FTS target observations showed a large enhancement that decreased with time after its initial blowout, because single-day and single-point data have large uncertainties in estimating the CH_4 leak quantitatively. In this study, we examined the utility of our partial-column CO_2 density retrievals to estimate emissions from megacities by using multiple-day data, which are assumed to constant with time.

Existing space-based spectrometers cover a limited area of Earth's surface when acquiring sufficient photons and spectral resolution to retrieve CO_2 precisely. Most anthropogenic CO_2 emissions are believed to originate from cities and point sources, which occupy a small percentage of Earth's surface. A crucial question regarding satellite operation is whether allocating observation resources to more city areas can improve the understanding of local flux. Since the global area coverage by GOSAT is less than 1% because TANSO-FTS uses one pixel in each band, and it has an acquisition time of 4.6 s, the resource allocation to target observations is limited. Therefore, we prioritized observation over global megacities. The simulated wind speed and emission inventory analyzed the partial-column CO_2 density data collected at several global megacities. We selected winter months (January-March) data when vertical convection and CO_2 uptake by plants were expected to be low. We used data from 2019 and 2020 to compare year- to-year variation.

In this study, Section 2 describes the partial-column density of LT by combining reflected sunlight with two orthogonal components of polarization and thermal emission data from TANSO-FTS. The target observation patterns sampled over the selected megacities are discussed in Section 2. Section 3 calculates the CO_2 concentration enhancement from the GOSAT retrieval data and characterizes the observed enhancements by using simulated wind speed and emission estimates from an emission inventory. Section 4 discusses the limitations of this study and future research directions.

2. GOSAT instruments, partial-column density retrievals for CO_2, and target observations

GOSAT employs the FTS technology to prioritize the multiplex advantage of wide spectral coverage and spectral resolution at the expense of imaging capability. The combination of reflective optics and a beam splitter made of an uncoated ZnSe can cover the spectral range from 0.76 μm in the near-infrared to 15 μm in the thermal infrared region to observe both reflected sunlight with two orthogonal components of polarization and thermal emissions simultaneously (Kuze et al., 2009). TANSO-FTS has three narrow shortwave infrared (SWIR) bands at 0.76 µm for oxygen (O_2), 1.6 µm for CO_2 and CH_4, and 2.0 µm for CO_2, and one wide thermal infrared (TIR) band with a spectral sampling interval of 0.2 cm^{-1}. All spectral bands have a common field stop to acquire a signal from the same geophysical location. The optical throughput advantage of FTS can collect sufficient photons to improve the signal-to-noise ratio with a circular footprint of 10.5 km in diameter.

A two-axis agile pointing system with onboard memory can observe wide cross-track (CT) areas and specify the observation locations with a pointing accuracy better than 1 km. GOSAT started the original grid observation with a three-day revisit cycle at a local time of 13:00. Since 2016, we have allocated more soundings for target observations over significant anthropogenic emission sources, such as megacities and CH_4 point emission sources (Kuze et al., 2016). When a satellite speed of 7 km/s, 4.6 s sampling interval, and a pointing range of ±20°, in the along-track (AT) and ±35° in CT, a maximum of 16 target locations are accessible within a city area in every orbit. In theory, GOSAT can cover 42 × 42 km^2 for intense square observations, as illustrated in Fig. 1. In November 2018, a solar-paddle-rotation incident occurred and was recovered by December. Since the TANSO-FTS observation restarted, pointing has been stable and accurate through 2019 and 2020, the period we selected for analysis in this study.

The National Institute for Environmental Studies (NIES) has developed and provided column density of CO_2 as operational GOSAT Level 2 product (Yoshida et al., 2013). Like many existing products (Butz et al., 2011; Parker et al., 2011, O'Dell et al., 2012, and Crisp et al., 2012), the NEIS product only uses radiance spectra from the three SWIR bands by combining two orthogonal components of polarization bands into single radiance spectra. Their products' standard deviation and bias of the CO_2 retrievals are 2.09 ppm or 0.5% and -1.48 ppm, respectively, when validated with the Total Carbon Column Observing Network (TCCON) column density data retrieved from the direct solar radiation on the ground (Wunch et al., 2011). Janardanan et al. (2016) used the NIES product for calculating concentration enhancement due to fossil fuel emissions using transport model simulations and reported potential biases in emission inventory estimates.

As a separate independent effort, we developed a retrieval algorithm for a partial column density of two tropospheric and three stratosphere layers and a total column density by combined use of the

SWIR and TIR bands by the maximum a posteriori solution method (Kikuchi et al., 2016). Kulawik et al. (2017) presented a retrieval method using the pressure broadening of the CO_2 absorption spectra in the GOSAT SWIR bands. Such analyses require accurate characterization of the instrument line shape function. Instead, we used the TIR radiance spectra of thermal radiation emitted from atmospheric CO_2 at different altitudes by simultaneously retrieving the vertical temperature gradient. The number of vertical layers was limited for obtain robust retrievals. We can obtain the difference between the CO_2 density of two individual layers of LT and UT (XCO_2^{LT} and XCO_2^{UT}) by constraining the total column density (XCO_2) accurately. Three stratosphere layers are used for converging retrieved partial-column densities.

We propose to estimate CO_2 emissions from megacities by calculating the enhancement in LT, where surface emission hotspots are located. The concept of simultaneous observations and our partial-column retrieval is illustrated in Fig. 1. Because scattering by aerosols and clouds is largely polarized and the surface reflection is less polarized than that, the independent use of two orthogonal components of polarization in the three SWIR bands allows us to remove aerosol and thin cloud contamination instead of the combined use of polarization spectra adopted by many other existing retrieval algorithms. We define each vertical layer by the retrieved surface pressure (P_{surf}) retrieved from the O_2 *A* band for each sampling point, rather than the retrieved vertical temperature with large uncertainty. The LT and UT partial-columns were defined as 0.6-1 P_{surf} and 0.2-0.6 P_{surf}, respectively. The sizes of the airmass of the LT and UT columns determined by retrieved P_{surf} are approximately the same. In the ocean case, the typical vertical range of the LT column is approximately 0-4 km. The degrees of freedom for the signal of XCO_2 and XCO_2^{LT} are typically 1.2 and 0.6, respectively. Retrieved XCO_2 was validated using TCCON data (Kikuchi et al., 2016). A subset of the retrieved XCO_2^{LT} was validated using spiral flight data over Railroad Valley in Nevada, USA (Tanaka et al., 2016). 49 spiral flights were performed from the surface (25 m or lower) to 8,500 m at the time of GOSAT overpasses. (https://www.eorc.jaxa.jp/GOSAT/GHGs_Vical/ghg_vical_trace_gas.html). The comparison shows that bias, standard deviation, and expected retrieval error for XCO_2^{UT} and ones for XCO_2^{LT} are 2.4, 1.6, 1,7, 1.1, 1.6, and 1.4 ppm, respectively. By assuming that the LT comprises the entire boundary layer in winter months, analysis using XCO_2^{LT} should allow us to focus on local emissions. Kuze et al. (2020) demonstrated the advantages of using the partial-column density product for detecting local CH_4 emissions from a point source.

Typically, 1000 sampling points (5% of the total daily GOSAT observation points) are allocated to target observations (Kuze et al., 2016). Since 2016, we have added more than 10 megacities (Beijing, Cairo, Dhaka, Istanbul, Mexico City, Mumbai, New Delhi, New York City, Riyadh, Tokyo, and Shanghai) and implemented revised target observations every six days with smaller spatial gaps. Each city has a maximum of 16 sampling locations per orbit. In this study, we focused on six megacities (Beijing, New Delhi, New York City, Riyadh, Tokyo, and Shanghai) where a sufficient number of clear-sky and successful retrievals was available (listed in Table 1). Fig. 2 shows the center of the GOSAT footprint over the selected megacities superimposed with emissions taken from the year 2020 version of the Open-source Data Inventory for Anthropogenic CO_2 (ODIAC) inventory (Oda and Maksyutov, 2011; Oda et al., 2018). Beijing and New Delhi have square areas with 4 × 4 intense sampling points to cover significant emission sources. New York City, Riyadh, and Shanghai have modified squares to avoid water bodies (e.g. bays and rivers), where the surface reflectance in SWIR is low. However, megacities with a widely spread pattern such as Greater Tokyo Area, tend to have sparse sampling points.

We retrieved XCO_2^{LT} and XCO_2^{UT} from the calibrated radiance spectra of Level 1 version 220 and analyzed the retrieved data between January 2019 and March 2020. First, we only used wintertime data because data from other seasons are expected to be heavily affected by vertical convection (thicker boundary layer) and carbon uptake by plant photosynthesis (Lauvaux et al., 2016; Miller et al., 2020). We also selected days when more than 40% of the sampling points were successfully retrieved.

3. Examining XCO_2^{LT} enhancement over megacities

3.1 GOSAT XCO_2^{LT} enhancement over megacities

Fig. 3 shows the target observation locations and spatial distribution of the monthly averaged XCO_2^{LT} in March 2019 in (a) Beijing, (b) New Delhi, (c) New York City, (d) Riyadh, (e) Shanghai, and

(f) Tokyo. Beijing and Shanghai exhibited high CO_2 concentrations above 420 ppm. We also obtained high CO_2 values over Tokyo, but the sampling density was extremely low compared to other megacities. The area-averaged enhancement in $\Delta XCO_2(i,d)^{LT}{}_{aave}$ of target city *i* and observation day *d* is defined by Eq. (1). To mitigate the impact of the annual CO_2 increase and seasonal variations, we used the monthly area-averaged $XCO_2(i,m)^{UT}{}_{amave}$ of month *m* calculated using Eq. (2) for a reference. Because $XCO_2{}^{UT}$ is much less impacted by local surface emissions compared to $XCO_2{}^{LT}$ and has smaller day-to-day variations, we used area and monthly averaged data. Notably, we assume that the boundary layer is below the UT and LT boundaries during the winter months. The advantage of partial-column products is that we define references for the concentration enhancement calculation from simultaneous observations.

$$\Delta XCO_2(i,d)^{LT}{}_{aave} = \sum_k^N (XCO_2(i,d,k)^{LT} / N - XCO_2(i,m)^{UT}{}_{amave}) \qquad \text{Eq. (1)}$$

$$XCO_2(i,m)^{UT}{}_{amave} = \sum_d^M \sum_k^N \frac{XCO_2(i,d)^{UT}{}_{aave}}{MN} \qquad \text{Eq. (2)}$$

where $XCO_2(i,m)^{UT}{}_{aave}$, *k*, and *N* denote the $XCO_2{}^{UT}$ monthly average over city *i*, the sampling point, and the total number of successfully retrieved data for the city, respectively. *M* is the number of clear-sky datasets per month after screening cloud-contaminated data.

To confirm our assumption that emissions from megacities remain within LT, we compared $XCO_2{}^{LT}$ to the transport model outputs from the CarbonTracker (Peters et al., 2007) and NICAM-TM (Niwa et al., 2011). The two models used the ODIAC inventory for prescribing fossil fuel emissions. In February 2018, the CarbonTracker 2019B model at a 3° × 2° resolution covering selected megacities showed that enhancements were located no higher than 600 hPa, as described in Appendix A1. The CarbonTracker model in August shows enhancement from the surface and a higher density inflow in the UT. NICAM-TM provides a 0.125° × 0.125° resolution spatial data and shows the local enhancement also within LT.

3.2 Relation between wind speed and emission estimates

We next examined the utility of XCO_2^{LT} for estimating emissions from megacities. Remote sensing from space offers the advantage of capturing a snapshot of the entire emissions. The local CO_2 emissions from the footprint of the satellite observations can be expressed using the relationship between CO_2 enhancement and wind speed using equation Eq. (3).

$$f_{CO_2} = \frac{A_p V}{L_s} \Delta XCO_2^{LT} \qquad \text{Eq. (3)}$$

where f_{CO_2}, A_p, V, L_s, and ΔXCO_2^{LT} denote CO_2 emissions from an emission source, LT partial air mass, wind speed, the distance between the emission source of the footprint and its downwind edge and enhancement by emissions, respectively. The city area is often much larger than a single GOSAT footprint. In addition, individual observational data has a significant random error. Therefore, we averaged the XCO_2^{LT} values of a single day within a city to reduce random errors and cover the entire emission plume. We did not consider within-city emission gradients. By detailing the relationship in Eq. (3) and considering the inflow from upwind locations, the XCO_2^{LT} enhancement over megacities from the GOSAT observations can be expressed with the following model for a spatially spread city area:

$$\Delta XCO_2(i,d)^{LT}{}_{aave} = \frac{F_{CO_2}(i,d) L_C(i)}{V_C(i,d) A_{Cp}(i)} + \Delta XCO_2(i)^{LT}{}_{upwind} \qquad \text{Eq. (4)}$$

where $F_{CO_2}(i,d)$, $L_C(i)$, $V_C(i,d)$, and $A_{Cp}(i)$ are the CO_2 emissions, the average distance between the center of the city area and the edge of the downwind, wind speed, and the partial air mass of LT for the selected area of city *i* and day *d*, respectively. We use the Hybrid Single-Particle Lagrangian Integrated Trajectory model (HYSPLIT) for $V_c(i,d)$ (Stein et al., 2015) as described in Appendix A2. $\Delta XCO_2(i)^{LT}{}_{upwind}$ is the LT enhancement upwind of city *i*.

Because $XCO_2\ (i.d)^{LT}$ enhancement is a function of emissions and the inverse of wind speed, we could use a least-square linear fit of the screened datasets for deriving emission estimates. We added one piece of virtual data with uncertainty of 5 ppm with infinite wind speed to constrain the linear fit. Fig. 4. The values are assumed to be constant in our study and estimated using the ODIAC inventory product and the typical wind direction in winter per HYSPLIT as described in Appendix A3. Table 2 shows relations by introducing the coefficient $\alpha(i) = F_{CO2}(i)L_C(i) / A_{Cp}(i)$ in Eq. (4) for the six selected megacities. The point of origin of the vertical axis represents the $\Delta XCO_2(i)^{LT}{}_{upwind}$, which is the level of infinite wind speed. Calculation methods using Eq. A3 to estimate emissions are described in Appendix A4. The uncertainty in $\alpha(i)$ was calculated using Eq. A4 from the uncertainty of $\triangle XCO_2(i.d)^{LT}$, which is modeled as a summation of the wind-speed-dependent error, retrieval error and inflow in Appendix A5. All six megacities show positive relations between megacity XCO_2^{LT} enhancement and the inverse of wind speed. Table 2 summarizes the coefficients $\alpha(i)$ for the six megacities and their uncertainties using the winter months (January–March) of 2019 and 2020. Errors due to averaging an inhomogeneous distribution of XCO_2^{LT} such as those for Riyadh are not included in the uncertainty assessment.

Beijing shows a good relationship between XCO_2^{LT} enhancement and wind speed among the six megacities with an uncertainty of 50% (listed in Table 2) and its emissions are high. The wind direction in the winter months is stable, and no large cities and upwind northwest. Many successful CO_2 retrievals achieved from a clear-sky dataset and an intense sampling pattern over the city minimized random errors. We assumed that both photosynthesis and vertical convection between UT and LT are low in winter. Another challenge is that 42 × 42 km^2 sampling is not wide enough to cover the entire megacity emission area, especially in the northeast, as shown in Fig. 2 (a) of the ODIAC inventory. For a more accurate estimation, the horizontal distribution of $\triangle XCO_2{}^{LT}$ must be considered. New Delhi also has a sampling pattern similar to that of Beijing. The estimated coefficient (3.5 ppm m/s) is lower than Beijing (21.1 ppm m/s) and has a much larger uncertainty. One of the possible reasons is that the uptake by photosynthesis cannot be ignored. Cloud-free scenes in New York City are minimal. Riyadh is an isolated city, but its emissions are lower than the uncertainty. Shanghai had the largest uncertainty. What contributed most to Shanghai's largest uncertainty were its lowest number of clear-sky datasets, the largest uncertainty in inflow due to other cities upwind (2.50 ppm), and the widely spread city. The city area of Tokyo is widely spread, and sparse sampling causes large uncertainty resulting in a large bias in emission estimation, even although 13 observations after screening cloud-contaminated data were available for analysis in winter 2019.

The analysis in the other seasons is expected to be more complicated than that in winter, possibly due to plant photosynthesis and vertical convection. We used Beijing, Riyadh, and Tokyo, which have a sufficient number of clear-sky datasets observations for analysis over both winter (>10) and year-round (>30) (listed in Table 1). Fig. 5 shows the relationship between CO_2 enhancement and wind speed using year-round data. The wind direction varies much more in the summer than in the other seasons, especially in Riyadh. All three megacities show lower coefficient of determination (R^2). Advanced analysis methods that consider meteorological information and biological activities are necessary for emission estimates for seasons other than winter.

The quantitative value of the averaged CO_2 emissions $F_{CO_2}(i)_{ave}$ from city i can be calculated from the coefficient $\alpha(i)$ expressed in Eq. (4). We used the partial air mass factor $A_{Cp}(i)$ for the entire city area. In the case of Beijing, the coefficient in Eq (4) is 21.1 ppm m/s in winter months 2019 and 2020, and the estimated emissions from the city area as defined in Fig. 2 (1) are 1.98 MtC/month/city.

To demonstrate the effectiveness of this analysis, we plotted the coefficient $\alpha(i)$ from XCO_2^{LT} enhancement for winter 2019 and 2020 separately. Fig. 6 shows the difference between winter months 2019 and winter months 2020, and Table 3 compares the estimated CO_2 emissions of winter 2019 and winter 2020 with nitrogen dioxide (NO_2) density averaged over the selected megacities. NO_2 is emitted together with high-temperature fossil fuel combustion, and its densities for selected megacities are calculated by averaging monthly data over the area defined in Fig. 2 acquired by the TROPOspheric Monitoring Instrument (TROPOMI) onboard the Sentinel-5 Precursor satellite (Veefkind et al, 2012). The data showed reductions in 2020 except for Riyadh NO_2. Analysis using a longer time period is necessary because the effect of economic slowdown due to COVID-19 differs among CO_2-relevant source sectors. For example, emissions from the transport sector were reduced, but emissions from power plants (the energy sector) did not change much (Le Quéré et al., 2020). The small change in New Delhi in 2020 may be due to the large-scale natural CO_2 changes, but the change is near the detection limit, and there is no clear evidence.

3.3 Comparison with the ODIAC inventory

A comparison with a CO_2 emission inventory provides an opportunity to demonstrate the effectiveness of the estimates using satellite data. The integrated emissions per month for each city are listed in Table 2. Fig. 7 presents the correlation between our estimated megacity emissions $\alpha(i)$ and area-integrated emission values from the ODIAC inventory $E_c(i)$ in Eq. A1 in Appendix A2. i denotes an individual city. We used the ODIAC inventory as a reference to characterize the obtained CO_2 enhancements. The calculated correlation coefficient (p) was 0.83. Megacities with a sufficient number of clear-sky datasets and various wind speeds, such as Beijing and Tokyo, presented a smaller uncertainties of 50% and 89% (Table 2) in coefficient $\alpha(i)$ than other megacities. Emission estimates for New York City and Shanghai have large uncertainties. Emission for Riyadh was possibly underestimated by averaging GOSAT data over a much wider area than the actual enhanced area. The result from the linear fitting shows that the bias was within the range of uncertainties, but the amounts are smaller than those in the ODIAC inventory. Possible cause of the difference is bias in the wind speed at 500 m by HYSPLIT in slow cases. The actual speed near the surface may be more complicated than that in the HYSPLIT simulation.

Conversely, the inflow contribution estimated from the intercept of relationship between XCO_2^{LT} enhancement and the inverse of wind speed was overestimated. There are no significant emission sources in upwind area in Beijing. The GOSAT footprint requires additional coverage over these areas to determine the inflow. Retrieval of ΔXCO_2^{LT} and ΔXCO_2^{UT} are partially-averaged. ODIAC emissions might have had a bias. Oda et al. (2019) reported that the typical emission uncertainty for the ODIAC inventory is 30‑40% over city areas.

4. Discussion

4.1 Current limitations for emission estimation.

We examined the information contained in XCO_2^{LT} from GOSAT target observations over selected global megacities. The uniqueness of our method is that by assuming that vertical convection is negligible, the partial-column density of the LT is usable for studying local emissions under the uncertainty of CO_2 retrieval. XCO_2^{UT} can be used for the background level estimate, which is difficult to determine using models or other methods accurately. A challenge is extending the analysis season to include summer when vertical convection is not negligible. Our analysis assumes that a wind speed of 500 m represents the plume motion, of which actual local dynamics are more complicated.

To improve the accuracy of our emission estimation, random errors and the bias of $\triangle XCO_2(i,d)^{LT}{}_{aave}$ in Appendix A5 must be reduced. In addition to observation uncertainties such as instrument noise and calibration uncertainties, the forward calculation of the radiative transfer in the atmosphere used in our retrieval method has both common bias and random errors. A major portion of errors were caused by uncertainties in absorption line parameters and light path modifications caused by aerosols and thin clouds. The current standard deviation S_r of the XCO_2^{LT} in our retrieval method described in Appendix A5 cannot be significantly reduced. Because single XCO_2^{LT} data had a large uncertainty even after averaging the data over a city area, we instead introduced a linear regression to estimate emissions from multiple-day data at various wind speeds. Vertical profiles of wind speed above a city are challenging to validate. They are regularly measured at limited locations such as airports. Instead, we tested the backward trajectory at the three heights of 500 m, 1000 m, and 2000 m above ground level (AGL) to represent the wind speed of plumes in LT. The coefficient of determination for emissions estimated from the density enhancement derived from Eq. 4 and wind speed $V_d(i,d)$ in Beijing are 0.33, 0.32, and 021 for AGL 500 m, AGL 1000 m, and AGL 2000 m, respectively. In this study, we used the wind speed at an AGL 500 m simulated by HYSPLIT. An additional upwind observation point can reduce the bias of $\Delta XCO_2(i,d)^{LT}{}_{inflow}$ in Eq. A6.

Among the megacities selected in this analysis, Beijing, Riyadh, and Tokyo have sufficient emissions exceeding the estimation limit (Table 2 and Fig. 7). Uncertainties for Tokyo and Riyadh are small because there was a sufficient number of clear-sky dataset: however, their sampling patterns have not been optimized. The sampling patterns of New York City and Shanghai require more points to be allocated and longer-term data should reduce the estimation uncertainty. New Delhi has a complicated flux, namely larger uptake than other 5 megacities, and emission enhancement is near the detection limit. The number of sampling points over Tokyo with various source sectors must be increased to cover the densely populated areas and industrial zones around Tokyo Bay.

4.2 Future perspectives and implications: GOSAT-2 and GOSAT-GW

This study focused on the utility of the enhancements calculated from the partial-column density. Based on what we obtained from, we suggest future applications for estimating emissions from megacities. Averaging with more sampling points per day and more frequent observations per month can reduce random errors in the estimation. More frequent observations will also provide various wind speeds that reduce estimate uncertainty. Instead of assuming a spatially uniform emission within the city, weighing the emission area and having a wider spatial coverage can mitigate the existing challenges by compromising the spatial and temporal resolutions of emission estimates. A wider spatial coverage can be applied to estimate inflow from other locations. TANSO-FTS-2 onboard GOSAT-2, which is the successor of GOSAT, has an advanced pointing system with an AT pointing range twice as wide as that of TANSO-FTS (Suto et al., 2021). It has started more intensive observations with 36 target points over Beijing to cover the entire emission and upwind areas (highlighted in Fig. 2). We have also added more sampling points to New York City to improve sampling density. The observation frequency is similar to that of GOSAT. This study does not use spatial distribution information with a GOSAT observation pattern, which assumes spatially uniform emission. Considering the spatial inhomogeneity of emission locations and their plumes within megacities, imaging spectrometers with higher spatial resolution and more sampling points such as OCO-3 are necessary (Kuze et al., 2019).

In our study, small enhancements of XCO_2^{LT} with a 10.5 km footprint is not sufficient to characterize the spatial distribution from the single-day observation data. Co-located short-lived NO_2 allows us to pinpoint source locations and depict emission plumes. Burdens between long-lived CO_2 and short-lived NO_2 are correlated (Fujinawa et al., 2021). The quantitative correlation between long-lived CO_2 and short-lived NO_2 shows significant uncertainty, but NO_2 distribution can help to make the spatial distribution of CO_2 enhancement more precisely. For example, the northern part of Beijing has significant NO_2 emissions acquired by the TROPOMI instrument and GOSAT data show higher enhancement in summer than that in other parts. TANSO-3 onboard GOSAT-GW has an imaging capability with a much higher spatial resolution than TANSO-FTS and TANSO-FTS-2. It simultaneously observes CO_2 and NO_2. However, our partial-column retrieval method cannot be applied, because it has no TIR band. Coincident observations by TANSO-FTS or TANSO-FTS-2 are required to obtain XCO_2^{LT}. A finer spatial distribution estimated from the NO_2 data will also provide sector information for individual sources. The classification of emissions from the source sectors is required to monitor human activity. Locations of major point sources such as power plants and steel factories are often known, but their emission amounts and spatial distributions at very fine resolutions (1 km or less) must be estimated from observations. Higher-resolution data from lower altitudes, such as that from aircraft, will further improve emission estimation from source sectors by combining data to detect and estimate fine-resolution emissions.

This study demonstrates the potential utility of partial-column data to estimate city-level emissions during the winter months from the GOSAT XCO_2^{LT} data. For year-round analysis, CO_2 uptake by photosynthesis should be considered. GOSAT also observes solar-induced chlorophyll fluorescence, but further studies are necessary for a quantitative discussion. Our future perspectives are to improve local and global flux estimation and reach better agreement with inventories and reported emissions. The spatial distributions of the existing inventory, which are often based on the assumptions of emission disaggregation (Oda et al. 2019), are other challenges. Global flux has been estimated by combining atmospheric greenhouse gases by satellites with an atmospheric composition transport model, but still has significant uncertainties due to satellite data, meteorology, and *a priori* information (Deng et al., 2014).

5. Conclusions

TANSO-FTS onboard GOSAT has a multiplex advantage that enables simultaneous observations of solar reflected light with two orthogonal components of polarization and thermal emissions. Using a full spectral range, we obtained XCO_2^{LT} enhancement with XCO_2^{UT} for a reference, which is twice as large as the enhancement often obtained from the existing column density. The agile pointing system of TANSO-FTS can target megacities with smaller spatial gaps between the soundings. We presented megacity XCO_2^{LT} enhancement from the time series of targeted GOSAT data over Beijing, New Delhi, New York City, Riyadh, Shanghai, and Tokyo and the linear relation with the inverse of the simulated wind speed. We estimated the emissions from Beijing with an uncertainty of 50% in winter by intensive observations with a significant high clear-sky ratio, and small upwind inflow. Uncertainties in emission estimation increase because of smaller number of clear-sky datasets, sparse sampling, contamination of inflow from other megacities and due to uptake by plant photosynthesis and vertical convection during other seasons. We also compared our estimates to data from the ODIAC inventory. These results demonstrate the utility of the new partial-column density retrievals for estimating megacity CO_2 emissions. We also discussed current limitations in obtaining robust emissions, such as limited data and atmospheric transport. To reduce random errors and bias, more frequent, wider coverage and a characterization of the spatial distribution within a city are necessary.

Acknowledgements

This study has been funded by the Japan Aerospace Exploration Agency (JAXA). GOSAT is a joint project of JAXA, the Ministry of the Environment and NIES. We thank Yosuke Niwa of NIES for providing the NICAM model and Shinsuke Funaki, Satoshi Matsuo and Mana Matsuda of the Space Engineering Development Co., Ltd. For their valuable suggestions. We thank JAXA/EORC for the GOSAT partial-column product obtained from https://www.eorc.jaxa.jp/GOSAT/GPCG/download/GOSAT/, ESA for the TROPOMI NO_2 data obtained from https://s5phub.copernicus.eu/dhus/#/home, and NOAA ESRL for CarbonTracker CT2019B obtained from http://carbontracker.noaa.gov. The ODIAC emission data product was obtained from the Global Environmental Database hosted by the Center for Global Research at NIES (https://db.cger.nies.go.jp/dataset/ODIAC/). We also used base maps from OpenStreetMap.

Appendix

Fig A1. Shows the flowchart of the study. The appendix describes the detailed analysis method used in this study.

A1. Comparison with CarbonTracker

We used the CarbonTracker 2019B model to confirm the enhancement distribution from a megacity in winter and summer. Because the data for 2019 and 2020 are not available, we used data from February and August 2018. Fig. A2 shows the vertical profiles of CO_2 at a local time of around 13:00. The model data show enhancement within LT, where a typical boundary is 600 hPa. Some of the Beijing data in August suggest the effect of vertical convection and uptake by plants.

A2. Wind speed and meteorology model

As shown by Eq. (3), XCO_2^{LT} enhancement is a function of CO_2 emissions and wind speed. Unfortunately, there were no vertical profile measurements of the wind to cover city areas of interest, and there were often only limited data available at airports. Thus, we used the HYSPLIT model to represent the wind over the selected megacities. HYSPLIT was driven by the Global Data Assimilation System (GDAS) 1° data at 1-h intervals. We also used the simulated wind for the backward trajectory to estimate the inflow from the upwind. Because of the low boundary layer in winter, we used the wind data at AGL 500 m to represent the transport.

A3. Calculating CO_2 emission estimates for selected megacities and inflow using an inventory

The ODIAC inventory distributes up-to-date country fossil fuel CO_2 emission estimates using power plant information and satellite-observed nightlights at 1×1 km^2 resolution (Oda and Maksyutov 2011, 2015, Oda et al., 2010; 2018; 2019). The ODIAC inventory was originally developed for CO_2 flux inversion analyses of GOSAT Level 4 product development (e.g., Oda and Maksyutov 2011; Maksyutov et al., 2013). Since its establishment, The ODIAC inventory has been used in global and regional traditional surface flux inversions (e.g., Takagi et al., 2011; Saeki et al., 2013; Houweling et al., 2015; Feng et al., 2017; Crowell et al., 2019; Palmer et al., 2019). The global high-resolution emission field in ODIAC has also been successfully used in city emission studies (e.g., Oda et al., 2013; Lauvaux et al., 2016; Hedelius et al.; 2018; Martin et al., 2018; Reuter et al., 2019; Wang et al., 2019; Wu et al., 2018; 2020; Yang et al., 2020; Ye et al., 2020; Ahn et al., 2020). Further details of the ODIAC inventory can be found elsewhere (Oda and Maksytuov 2011; Oda et al., 2010; 2018; 2019).

To compare the megacity emission estimate obtained from the GOSAT data, we aggregated the 1×1 km^2 emissions to a 0.1° × 0.1°, summed up the emission values over the city areas defined in Fig. 2 and calculated the total carbon emission per month $E_c(i)$ for selected city *i* by using the following equation:

$$E_C(i) = \sum_{lon}\sum_{lat} E_{ODIAC}(lat, lon) \qquad \text{Eq. A1,}$$

where $E_{ODIAC}(lat,lon)$ is the carbon emission per 0.1° cell (ton C/cell). The area in Fig. 2 shows the coverage of the GOSAT footprints and the surrounding city area upwind. The number of ODIAC cells used in these calculations for Beijing, New Delhi, New York City, Riyadh, Shanghai, and Tokyo were 25, 20, 21, 20, 22, and 39, respectively. The city area of greater Tokyo is widely spread and GOSAT sampling spatial density is sparser than that in other megacities. We integrated a wider area but excluded the industrial area in the southeast, located downwind of the city.

The inflow in LT to the selected area creates a positive bias in calculating the XCO_2^{LT} enhancement in the selected city. We calculated the background level for a selected city far upwind by using the ODIAC inventory and a simple contribution model that is constant over time. The wind direction for this calculation for each city is that most frequently used by the HYSPLIT backward trajectory in the winter months (listed in Table 1). The wind direction was stable in winter, with a variation of 20°. Observation points upwind are too sparse, and we do not estimate the inflow solely from the GOSAT data. We integrated the ODIAC inventory under the backward trajectory by using HYSPLIT to estimate inflow. The area for integration is between the edge of the city area and 540 km from the city center, which is 10 times larger than the diagonal distance of the selected city area. The integrated area had a sector angle of 20°. The inflow model portion in $\Delta XCO_2(i)^{LT}{}_{upwind}$ is calculated using the following equation: the apex of the sector is located at the edge of the city, where the GOSAT footprint is 10.5 km wide.

$$\Delta XCO_2(i,d)^{LT}{}_{inflow} = \gamma \sum_{lon} \sum_{lat} \eta(l) E_{Odiac}(lat,lon) \qquad \text{Eq. A2,}$$

Where $\eta(l)$ is the contribution from the emission source along the trajectory as a function of the distance l from the center of the city (defined in Fig. 2), which becomes zero at 540 km. Hubeny's distance formula was used to calculate distance. γ is the conversion factor from the amount of CO_2 inflow to the partial-column density of LT over the selected city considering its LT air mass and assuming that inflow remains for 1 h within a city. The cross-section spreads as the distance increases and is normalized by a Gaussian curve. Fig. A3 shows the area of integration and emission distribution. The calculated results are presented in Table 2.

A4. Estimated emission and its uncertainty

We estimated the emissions by using a least-square fit of enhancement $\Delta XCO_2(i,d)^{LT}{}_{aave}$ and the inverse of wind speed $V_d(i,d)$. The linear slope and its uncertainty were calculated using Eqs. A3 and A4. The uncertainties $s_d(i,d)$ in $\Delta XCO_2(i,d)^{LT}{}_{aave}$ are functions of wind speed, retrieval error, and inflow (described in Appendix A5).

$$\alpha(i) = \frac{1}{W_i}\left(\sum_d^Y \frac{1}{s_d(i,d)^2} \sum_d^Y \frac{\Delta XCO_2(i,d)^{LT}{}_{aave}}{V_d(i,d)s_d(i,d)^2} - \sum_d^Y \frac{\Delta XCO_2(i,d)^{LT}{}_{aave}}{s_d(i,d)^2} \sum_d^Y \frac{1}{V_d(i,d)s_d(i,d)^2} \right) \quad \text{Eq. A3.}$$

$$\Delta\alpha(i) = sqrt\left(\frac{1}{W_i}\sum_d^Y \frac{1}{s_d(i,d)^2}\right) \quad \text{Eq. A4}$$

where $W_i = \sum_d^Y \frac{1}{s_d(i,d)^2} \sum_d^Y \frac{1}{V_d(i,d)^2 s_d(i,d)^2} - \left(\sum_d^Y \frac{1}{V_d(i,d)s_d(i,d)^2} \right)^2$.

For Eq. A5, the LT enhancement upwind for each city can also be calculated as the intercept of infinite speed, which is larger than that calculated in Appendix A2.

$$\Delta X_{LT}CO_2(i)^{LT}{}_{upwind} = \frac{1}{W_i}\left(\sum \frac{\Delta X\ CO_2(i,d)^{LT}{}_{aave}}{s_d(i,d)^2} \sum \frac{1}{V_d(i,d)^2 s_d(i,d)^2} - \sum \frac{1}{V_d(i,d)s_d(i,d)^2} \sum \frac{\Delta XCO_2(i,d)^{LT}{}_{aave}}{V_d(i,d)s_d(i,d)^2} \right) \quad \text{Eq. A5.}$$

A5. Uncertainty in the XCO_2^{LT} enhancement

Wind speed simulation models of the global scale with a 1° grid can be justified in a geostrophic wind condition, and they generally has a large uncertainty, especially for slower wind speeds. We apply the least-square fit with errors to estimate emissions from a city (described in Section 3.2). We converted the wind speed-dependent error to uncertainty in $\triangle XCO_2(i.d)^{LT}{}_{aave}$ for each day. The uncertainty $s_d(i,d)$ of city *i* and day *d* associated with wind speed dependency, retrieval errors s_r in XCO_2^{LT}, and the inflow of each day and city (described in Appendices A2 and A3) are expressed as follows:

$$s_d(i,d) = {}^{s_w}\!\!\Big/\!\sqrt{V_d(i,d)} + s_r + \Delta XCO_2(i,d)^{LT}{}_{inflow} \quad \text{Eq. A6,}$$

where S_w denotes uncertainty when wind speed is 1 m/s. Fig. A4. shows the uncertainty model used in this study as a function of wind speed. S_r is the standard deviation of the difference between XCO_2^{LT} and XCO_2^{UT} and remains constant at $2.09 \times \sqrt{2} = 3.0$ ppm, assuming the standard deviation of the partial-column product is 2.09 ppm. More vertical profile data using aircrafts and radiosondes for characterizing random errors and bias are necessary for a future quantitative estimation.

References

Ahn, D., Hansford, J. R., Howe, S., Ren, X. R., Salawitch, R. J., Zeng, N., Cohen, M. D., Stunder, B., Salmon, O. E., Shepson, P. B., Gurney, K. R., Oda, T., Karion, A., Lopez-Coto, I., Whetstone, J., Dickerson, R. R., 2020. Fluxes of Atmospheric Greenhouse-Gases in Maryland (FLAGG-MD): Emissions of Carbon Dioxide in the Baltimore, MD-Washington, D.C. area, *J. Geophys. Res. Atmos.* https://doi.org/10.1029/2019JD032004.

Brioude, J., Angevine, W. M., Ahmadov, R., Kim, S.-W., Evan, S., McKeen, S. A., Hsie, E.-Y., Frost, G. J., Neuman, J. A., Pollack, I. B., Peischl, J., Ryerson, T. B., Holloway, J., Brown, S. S., Nowak, J. B., Roberts, J. M., Wofsy, S. C., Santoni, G. W., Oda, T., Trainer, M., 2013. Top-down estimate of surface flux in the Los Angeles Basin using a mesoscale inverse modeling technique: assessing anthropogenic emissions of CO, NOx and CO_2 and their impacts, *Atmos. Chem. Phys.*, *13*, 3661–3677. https://doi.org/10.5194/acp-13-3661-2013.

Butz, A., Guerlet, S., Hasekamp, O., Schepers, D., Galli, A., Aben, I., Frankenberg, C., Hartmann, J.-M., Tran, H., Kuze, A., Keppel-Aleks, G., Toon, G., Wunch, D., Wennberg, P., Deutscher, N., Griffith, D., Macatangay, R., Messerschmidt, J., Notholt, J., and Warneke, T., 2011. Toward accurate CO_2 and CH_4 observations from GOSAT, *Geophys. Res. Lett., 38*, L14812, https://doi:10.1029/2011GL047888.

Crowell, S., Baker, D., Schuh, A., Basu, S., Jacobson, A. R., Chevallier, F., Liu, J., Deng, F., Feng, L., McKain, K., Chatterjee, A., Miller, J. B., Stephens, B. B., Eldering, A., Crisp, D., Schimel, D., Nassar, R., O'Dell, C. W., Oda, T., Sweeney, C., Palmer, P. I., Jones, D. B. A., 2019. The 2015–2016 carbon cycle as seen from OCO-2 and the global in situ network, *Atmos. Chem. Phys.*, *19*, 9797–9831. https://doi.org/10.5194/acp-19-9797-2019.

Crisp,D., Atlas, R. M., Bréon, F.-M., Brown, L. R., Burrows, J. P., Ciais, P., Connor, B. J.,Doney, S. C., Fung, I. Y., Jacob, D. J., Miller, C. E., O'Brien, D., Pawson, S., Randerson, J. T., Rayner, P., Salawitch, R. J., Sander, S. P., Sen, B., Stephens, G.L., Tans, P. P., Toon, G.C., Wennberg, P. O., Wofsy, S. C., Yung, Y. L., Kuang, Z., Chudasama, B., Sprague, G., Weiss, B., Pollock, R., Kenyon, D., Schroll, S., 2004. The orbiting carbon observatory (OCO) mission. *Adv. Space Res.*, *34*, 700–709. http://dx.doi.org/10.1016/j.asr.2003.08.062.

Crisp, D., Fisher, B. M., O'Dell, C., Frankenberg, C., Basilio, R., Boesch, H. L., Brown, R., Castano, R., Connor, B., Deutscher, N. M., Eldering, A., Griffith, D., Gunson, M., Kuze, A., Mandrake, L., McDuffie, J., Messerschmidt, J., Miller, C. E., Morino, I., Natraj, V., Notholt, J., O'Brien, D. M., Oyafuso, F., Polonsky, I., Robinson, J., Salawitch, R., Sherlock, V., Smyth, M., Suto, H., Taylor, T. E., Thompson, D. R., Wennberg, P. O., Wunch, D., Yung, Y. L., 2012. The ACOS CO_2 retrieval algorithm – part II: global XCO_2 data characterization. *Atmos. Meas. Tech.*, *5*, 687–707. https://doi.org/10.5194/amt-5-687-2012.

Crisp, D., et al., 2018, A constellation architecture for monitoring carbon dioxide and methane from space. *CEOS Atmospheric Composition Virtual Constellation*, 1, 164 pp, http://ceos.org/document_management/Virtual_Constellations/ACC/Documents/CEOS_AC-VC_GHG_White_Paper_Version_1_20181009.pdf.

Davis, K. J., Deng, A., Lauvaux, T., Miles, N. L., Richardson, S. J., Sarmiento, D. P., Gurney, K. R., Hardesty, M., Bonin, T. A., Brewer, W. A., Lamb, B. K., Shepson, P. B., Harvey, R. M., Cambaliza, M. O., Sweeney, C., Turnbull, J. C., Whetstone, J., Karion. A., 2017. The Indianapolis Flux Experiment (INFLUX): A test-bed for developing urban greenhouse gas emission measurements. *Elementa: Science of the Anthropocene*, *5*, 21. https://doi.org/10.1525/elementa.188.

Deng, F., Jones, D. B. A., Henze, D. K., Bousserez, N., Bowman, K. W., Fisher, J. B., Nassar, R., O'Dell, C., Wunch, D., Wennberg, P. O., Kort, E. A., Wofsy, S. C., Blumenstock, T., Deutscher, N. M., Griffith, D. W. T., Hase, F., Heikkinen, P., Sherlock, V., Strong, K., Sussmann, R., T. Warneke, 2014. Inferring regional sources and sinks of atmospheric CO_2 from GOSAT XCO_2 data, *Atmos. Chem. Phys.*, *14*, 3703–3727. https://doi.org/10.5194/acp-14-3703-2014.

Eldering, A., Taylor, T. E., O'Dell, C. W., Pavlick, R., 2019. The OCO-3 mission: measurement objectives and expected performance based on 1 year of simulated data, *Atmos. Meas. Tech.*, *12*, 2341–2370, https://doi.org/10.5194/amt-12-2341-2019.

Feng, L., Palmer, P. I., Bösch, H., Parker, R. J., Webb, A. J., Correia, C. S. C., Deutscher, N. M., Domingues, L. G., Feist, D. G., Gatti, L. V., Gloor, E., Hase, F., Kivi, R., Liu, Y., Miller, J. B., Morino, I., Sussmann, R., Strong, K., Uchino, O., Wang, J., Zahn, A., 2017. Consistent regional fluxes of CH_4 and CO_2 inferred from GOSAT proxy XCH_4: XCO_2 retrievals, 2010–2014. *Atmos. Chem. Phys.*, *17*, 4781–4797, https://doi.org/10.5194/acp-17-4781-2017.

Fujinawa., T., Kuze A., Suto, H., Shiomi, K., Kanaya, Y., Kawashima, T., Kataoka, F., Mori, S., Eskes H., Tanimoto, H., 2021. First concurrent observations of NO_2 and CO_2 from Power Plant Plumes by Airborne Remote Sensing, *Geophys. Res. Lett.*, *48,* e2021GL092685, https://doi.org/10.1029/2021GL092685.

Ganesan, A. L., Rigby, M., Lunt, M. F., M. F., Parker, R. J., Boesch, H., Goulding, N., Umezawa, T., Zahn, A., Chatterjee, A., Prinn, R. G. Tiwari, Y. K., van der Schoot M., Krummel P. B., , 2017. Atmospheric observations show accurate reporting and little growth in India’s methane emissions. *Nat. Commun*., 8, 836. https://doi.org/10.1038/s41467-017-00994-7.

Ganshin, A., Oda, T., Saito, M., Maksyutov, S., Valsala, V., Andres, R. J., Fisher, R. E., Lowry, D., Lukyanov, A., Matsueda, H., Nisbet, E. G., Rigby, M., Sawa, Y., Toumi, R., Tsuboi, K., Varlagin, A., Zhuravlev, R., 2012. A global coupled Eulerian-Lagrangian model and 1 × 1 km CO_2 surface flux dataset for high-resolution atmospheric CO_2 transport simulations, *Geosci. Model Dev.*, *5*, 231–243. https://doi.org/10.5194/gmd-5-231-2012.

Hedelius, J. K., Liu, J., Oda, T., Maksyutov, S., Roehl, C. M., Iraci, L. T., Podolske, J. R., Hillyard, P. W., Liang, J., Gurney, K. R., Wunch, D., Wennberg, P. O., 2018. Southern California megacity CO_2, CH_4, and CO flux estimates using ground- and space-based remote sensing and a Lagrangian model, *Atmos. Chem. Phys.*, *18*, 16271–16291. https://doi.org/10.5194/acp-18-16271-2018.

Hirabayashi, T., 2020. Contribution of JAXA’s Earth Observation Missions to Water Cycle and Climate Studies, Disaster Mitigation, and Operational Applications, EGU General Assembly 2020, EGU2020-19165. https://doi.org/10.5194/egusphere-egu2020-19165.

Houweling, S., Baker, D., Basu, S., Boesch, H., Butz, A., Chevallier, F., Deng, F., Dlugokencky, E.J., Feng, L., Ganshin, A., Hasekamp, O., Jones, D., Maksyutov, S., Marshall, J., Oda, T., O’Dell, C.W., Oshchepkov, S., Palmer, P. I., Peylin, P., Poussi, Z., Reum, F., Takagi, H., Yoshida, Y., Zhuravlev, R., 2015. An intercomparison of inverse models for estimating sources and sinks of CO_2 using GOSAT measurements. *J. Geophys. Res. Atmos.*, *120*, 5253–5266. https://doi.org/10.1002/2014JD022962.

Intergovernmental Panel on Climate Change, 2019. 2019 Refinement to the 2006 IPCC Guidelines for National Greenhouse Gas Inventories. ISBN 978-4-88788-232-4.

Janardanan, R., Maksyutov, S., Oda, T., Saito, M., Kaiser, J. W., Ganshin, A., Stohl, Q., Matsunaga, T., Yoshida, Y., Yokota, T., 2016. Comparing GOSAT observations of localized CO_2 enhancements by large emitters with inventory-based estimates, *Geophys. Res. Lett.*, *43,* 3486–3493. https://doi.org/10.1002/2016GL067843.

Jacob, D. J., Turner, A. J., Maasakkers, J. D., Sheng, J., Sun, K., Liu, X., Chance, K., Aben, I., McKeever, J., Frankenberg, C., 2016. Satellite observations of atmospheric methane and their value for quantifying methane emissions, *Atmos. Chem. Phys.*, *16*, 14371–14396, https://doi.org/10.5194/acp-16-14371-2016.

Kiel, M., Eldering, A., Roten, D. D., Lin, J. C. Feng, S., Lei, R., Lauvaux, T., Oda, T., Roehl, C. M., Blavier, J., Iraci, L. T., 2021. Urban-focused satellite CO_2 observations from the Orbiting Carbon Observatory-3: A first look at the Los Angeles megacity, *Remote Sens. Env.*, *258*, https://doi.org/10.1016/j.rse.2021.112314.

Kikuchi, N., Yoshida, Y., Uchino, O., Morino, I., Yokota, T., 2016. An advanced retrieval algorithm for greenhouse gases using polarization information measured by GOSAT TANSO-FTS SWIR I: Simulation study, *J. Geophys. Res. Atmos*., *121*. https://doi.org/10.1002/2015JD024720.

Kort, E. A., Frankenberg, C., Miller, C. E., Oda, T., 2012. Space-based Observations of Megacity Carbon Dioxide, *Geophys. Res. Lett.*, *39*, L17806. https://doi.org/10.1029/2012GL052738.

Kulawik, S. S., O'Dell, C., Payne, V. H., Kuai, L., Worden, H. M., Biraud, S. C., Sweeney, C., Stephens, B., Iraci, L. T., Yates, E. L., Tanaka, T., 2017. Lower-tropospheric CO_2 from near-infrared ACOS-GOSAT observations, *Atmos. Chem. Phys.*, *17*, 5407–5438. https://doi.org/10.5194/acp-17-5407-2017.

Kuze, A., Suto, H., Nakajima, M., Hamazaki, T., 2009. Thermal and near infrared sensor for carbon observation Fourier-transform spectrometer on the Greenhouse Gases Observing Satellite for greenhouse gases monitoring, *Appl. Opt.*, *48*, 6716–6733. https://doi.org/10.1364/AO.48.006716.

Kuze, A., Suto, H. Shiomi, K. Kawakami, S. Tanaka, M., Ueda, Y., Deguchi, A., Yoshida, J., Yamamoto, Y., Kataoka, F., Taylor, T. E., Buijs, H. L., 2016. Update on GOSAT TANSO-FTS performance, operations, and data products after more than 6 years in space, *Atmos. Meas. Tech.*, *9*, 2445–2461, https://doi.org/10.5194/amt-9-2445-2016.

Kuze A., Suto H., 2019. Imaging spectrometer suite for monitoring the Anthropocene Remotely from space, 5891, IGARSS 2019 - 2019 IEEE International Geoscience and Remote Sensing Symposium. https://doi:10.1109/IGARSS.2019.8900131.

Kuze, A., Kikuchi, N., Kataoka, F., Suto, H., Shiomi, K., Kondo, K., 2020. Detection of Methane Emission from a Local Source Using GOSAT Target Observations, *Remote Sens*, *12* (2), 267. https://doi.org/10.3390/rs12020267.

Lauvaux, T., Miles, N. L., Deng, A., Richardson, S. J., Cambaliza, M. O., Davis, K. J., Gaudet, B., Gurney, K. R., Huang, J., O'Keefe, D., Song, Y., Karion, A., Oda, T., Patarasuk, R., Razlivanv, I., Sarmiento, D., Shepson, P., Sweeney, C., Turnbull, J., Wu, K., 2016. High-resolution atmospheric inversion of urban CO_2 emissions during the dormant season of the Indianapolis Flux Experiment (INFLUX), *J. Geophys. Res. Atmos.*, *121*, 5213–5236. https://doi.org/10.1002/2015JD024473.

Le Quere, L., Jackson, R. B.., Jones, M. W., Smith, A. J. P., Abernethy, S., Andrew R. M.,De-Gol1, A. J., Willis, D. R., Shan. Y., Canadell, J. G., Friedlingstein, P., Creutzig, F., Peters, G. P., 2020. Temporary reduction in daily global CO_2 emissions during the COVID-19 forced confinement. *Nat. Clim. Chang. 10*, 647–653. https://doi.org/10.1038/s41558-020-0797-x.

Maksyutov, S., Takagi, H., Valsala, V. K., Saito, M., Oda, T., Saeki, T., Belikov, D. A., Saito, R., Ito, A., Yoshida, Y., Morino, I., Uchino, O., Andres, R. J., Yokota, T., 2013. Regional CO_2 flux estimates for 2009-2010 based on GOSAT and ground-based CO_2 observations, *Atmos. Chem. Phys.*, *13*, 9351-9373. https://doi:10.5194/acp-13-9351-2013.

Maksyutov, S., Oda, T., Saito, M., Janardanan, R., Belikov, D., Kaiser, J. W., Zhuravlev, R., Ganshin, A., Valsala, V. K., Andrews, A., Chmura, L., Dlugokencky, E., Haszpra, L., Langenfelds, R. L., Machida, T., Nakazawa, T., Ramonet, M., Sweeney, C., Worthy, D., 2021. Technical note: A high-resolution inverse modelling technique for estimating surface CO_2 fluxes based on the NIES-TM – FLEXPART coupled transport model and its adjoint, *Atmos. Chem. Phys.*, *21*, 1245–1266. https://doi.org/10.5194/acp-21-1245-2021.

Martin, C. R., Zeng, N., Karion, A., Mueller, K., Ghosh, S., Lopez-Coto, I., Gurney, K. R., Oda, T., Prasad, K., Liu, Y., Dickerson, R.R., Whetstone, J., 2018. Investigating Sources of Variability and Error in Simulations of Carbon Dioxide in an Urban Region, *Atmospheric Environment, 199*, 55-69. https://doi.org/10.1016/j.atmosenv.2018.11.013.

Matsunaga, T., Maksyutov, S., 2018. A guidebook on the use of satellite greenhouse gases observation data to evaluate and improve greenhouse gas emission inventories, national institute for environmental studies, Japan.

Mays, K. L., Shepson, P. B., Stirm, B. H., Karion, A., Sweeney, C., Gurney, K. R., 2009. Aircraft-based Measurements of the Carbon Footprint of Indianapolis, *Environ. Sci. Technol.*, *43*, 7816-7823. https://doi.org/10.1021/es901326b.

Mueller, K., Yadav, V., Lopez-Coto, I., Karion, A., Gourdji, S., Martin, C., Whetstone, J., 2018. Siting background towers to characterize incoming air for urban greenhouse gas estimation: A case study in the Washington, DC/Baltimore area. *J. Geophy. Res. Atmos.*, *123*, 2910– 2926. https://doi.org/10.1002/2017JD027364.

Miller, J. B., Lehman, S.J., Verhulst, K. R., Miller, C.E., Duren, R.M., Yadav, V., Newman, S., Sloop, S.D., 2020. Large and seasonally varying biospheric CO_2 fluxes in the Los Angeles megacity revealed by atmospheric radiocarbon, *Proc. Natl. Acad. Sci.*, *117* (43) 26681-26687. https://doi.org/10.1073/pnas.2005253117.

Nassar, R., Hill, T. G., McLinden, C. A., Wunch, D., Jones, D. B. A., Crisp, D., 2017. Quantifying CO_2 emissions from individual power plants from space. *Geophysical Research Letters*, *44*, 10,045–10,053. https://doi.org/10.1002/2017GL074702.

Niwa, Y., Tomita, H., Satoh, M., Imasu, R., A Three-Dimensional Icosahedral Grid Advection Scheme Preserving Monotonicity and Consistency with Continuity for Atmospheric Tracer Transport, 2011. *J. Meteorol. Soc. Jpn., 89*, 255–268. https://doi.org/10.2151/jmsj.2011-306.

Oda T, Maksyutov, S, Elvidge C. D., 2010. Disaggregation of national fossil fuel CO_2 emissions using a global power plant database and DMSP nightlight data. *Proc. of the Asia Pacific Advanced Network*, *30*, 220-229. http://dx.doi.org/10.7125/APAN.30.24.

Oda, T., Maksyutov, S., 2011. A very high-resolution (1 km×1 km) global fossil fuel CO_2 emission inventory derived using a point source database and satellite observations of nighttime lights. *Atmos. Chem. Phys. 11*, 543-556. https://doi.org/10.5194/acp-11-543-2011.

Oda, T, Ganshin, A., Saito, M., Andres, R. J., Zhuravlev, R., Sawa, Y., Fisher, R. E., Rigby, M., Lowry, D., Tsuboi, K., Matsueda, H., Nisbet, E. G., Toumi, R., Lukyanov, A, Maksyutov, S., 2013. The Use of a High-Resolution Emission Data Set in a Global Eulerian-Lagrangian Coupled Model, in Lagrangian Modeling of the Atmosphere (eds J. Lin, D. Brunner, C. Gerbig, A. Stohl, A. Luhar, P. Webley), American Geophysical Union, Washington, D. C. https://doi.org/10.1029/2012GM001263.

Oda, T, Maksyutov, S, 2015. ODIAC Fossil Fuel CO_2 Emissions Dataset, Center for Global Environmental Research, National Institute for Environmental Studies. https://doi:10.17595/20170411.001.

Oda, T., Maksyutov, S., Andres, R. J., 2018. The open-source data inventory for anthropogenic CO_2, version 2016 (ODIAC2016): A global monthly fossil fuel CO_2 gridded emissions data product for tracer transport simulations and surface flux inversions. *Earth Sys. Sci. Data*, *10* (1), 87–107. https://dx.doi.org/10.5194/essd10872018.

Oda, T., Bun R, Kinakh, V., Topylko, P., Halushchak, M., Marland, G., Lauvaux, T., Jonas, M., Maksyutov, S., Nahorski, Z., Lesiv, M., Danylo, O., Horabik-Pyzel, J., 2019. Errors and uncertainties in a gridded carbon dioxide emissions inventory. *Mitig Adapt Strat Gl. 24* (6): 1007-1050. https://doi.org/10.1007/s11027-019-09877-2.

O'Dell, C. W., Connor, B, Bősch, H, O'Brien, D, Frankenberg, C, Castano, R, Christi, M, Crisp, D, Eldering, A, Fisher, B, Gunson, M, McDuffie, J, Miller, C. E., Natraj, V., Oyafuso, F., Polonsky, I., Smyth, M., Taylor, T., Toon, G. C., Wennberg, P. O., and Wunch, D., 2012. The ACOS CO_2 retrieval algorithm –Part 1: Description and validation against synthetic observations, *Atmos. Meas. Tech., 5, 99-121.* https://doi.org/10.5194/amt-5-99-2012.

Pacala, S. W., et al., 2010. Verifying Greenhouse Gas Emissions: Methods to Support International Climate Agreements. Committee on Methods for Estimating Greenhouse Gas Emissions; National Research Council, National Academy of Sciences, 124pp. https://doi.org/10.17226/12883.

Palmer, P.I., Feng, L., Baker, D. Chevallier, F., Bösch, H., Somkuti, P., 2019. Net carbon emissions from African biosphere dominate pan-tropical atmospheric CO_2 signal. *Nat. Commun.* 10, 3344. https://dx.doi.org/10.1038/s41467-019-11097-w.

Parker, R., Boesch, H., Cogan, A., Fraser, A., Feng, L., Palmer, P.I., Messerschmidt, J., Deutscher, N., Griffith, D. W.T., Notholt, J., Wennberg, P. O., and Wunch, D., 2011. Methane observations from the Greenhouse Gases Observing SATellite: Comparison to ground–based TCCON data and model calculations, *Geophys. Res. Lett., 38*, L15807, https://doi:10.1029/2011GL047871.

Peters, W., Jacobson, A. R., Sweeney, C., Andrews, A. E., Conway, T. J., Masarie, K., Miller, J. B., Bruhwiler, L. M. P., Pétron, G., Hirsch, A. I., Worthy, D. E. J., van der Werf, G. R., Randerson, J. T., Wennberg, P. O., Krol, M. C., Tans, P. P., 2007. An atmospheric perspective on North American carbon dioxide exchange: CarbonTracker, *Proc. Natl. Acad. Sci.*, *104* (48), 18925-18930. https://doi.org/10.1073/pnas.0708986104.

Pinty, B., Janssens-Maenhout, G., Dowell, M., Zunker, H., Brunhes, T., Ciais, P., Dee, D., Denier van der Gon, H., Dolman, H., Drinkwater, M., Engelen, R., Heimann, M., Holmlund, K., Husband, R., Kentarchos, A., Meijer, Y., Palmer. P., Scholze, M. 2017. An Operational Anthropogenic CO_2 Emissions Monitoring & Verification Support capacity – Baseline Requirements, Model

Components and Functional Architecture. Report from the CO_2 Monitoring Task Force – sub-task B. European Commission Joint Research Centre, 25 EUR 28736 EN, https://dx.doi.org/10.2760/08644.

Ren, X., Salmon, O. E., Hansford, J. R., Ahn, D., Hall, D., Benish, S. E., Stratton, P. R., He., H., Sahu, S., Grimes,C., Heimburger, A. M. F., Martin, C. R., Cohen,M. D., Stunder, B., Salawitch, R. J., Ehrman, S. H., Shepson, P. B., Dickerson, R. R., 2018. Methane emissions from the Baltimore-Washington area based on airborne observations: Comparison to emissions inventories. *J. Geophy. Res. Atmos.*, 123, 8869– 8882. https://doi.org/10.1029/2018JD028851.

Reuter, M., Buchwitz, M., Schneising, O., Krautwurst, S., O'Dell, C. W., Richter, A., Bovensmann, H., Burrows, J. P., 2019. Towards monitoring localized CO_2 emissions from space: co-located regional CO_2 and NO_2 enhancements observed by the OCO-2 and S5P satellites, *Atmos. Chem. Phys*., *19*, 9371–9383. https://dx.doi.org/10.5194/acp-19-9371-2019.

Saeki, T., Maksyutov, S., Saito, M., Valsala, V. Oda, T., Andres, R. J., Belikov, D., Tans, P., Dlugokencky, E., Yoshida, Y., Morino, I., Uchino, O., Yokota, T., 2013. Inverse Modeling of CO_2 Fluxes Using GOSAT Data and Multi-year Ground-based Observations, *SOLA, 9*, 45-50. https://doi.org/10.2151/sola.2013-011.

Sargent, M., Barrera, Y., Nehrkorn, T., Hutyra, L. R., Gately, C. K., Jones, T., McKain, K., Sweeney, C., Hegarty, J., Hardiman, B., Wang, J.A., Wofsy, S. C., 2018. Anthropogenic and biogenic CO_2 fluxes in the Boston urban region, *Proc. Natl. Acad. Sci.*, *115* (29) 7491-7496. https://doi.org/10.1073/pnas.1803715115.

Schwandner, F. M., Gunson, M. R., Miller, C. E., Carn, S. A., Eldering, A., Kring, T., Verhulst, K. R., Schimel, D. S., Nguyen, H. M., Crisp, D., O'Dell, C. W., Osterman, G.B., Iraci, L. T., Podolske J. R., 2017. Spaceborne detection of localized carbon dioxide sources. *Science, 358* (6360), eaam5782, https://dx.doi.org/10.1126/science.aam5782.

Schuh, A. E., Otte, M., Lauvaux, T., Oda, T. , 2021. Far-fiel Biogenic and Anthropogenic Emissions as a Dominant Source of Variability in Local Urban Carbon Budgets: A Global High-Resolution

Model Study with Implications for Satellite Remote Sensing. *Remote Sens. Env.*, *258*, *Remote Sensing of Environment*. https://doi.org/10.1016/j.rse.2021.112473.

Sierk, B., Bézy, J. L., Löscher, A., Meijer, Y., 2019. The European CO_2 Monitoring Mission: observing anthropogenic greenhouse gas emissions from space, International Conference on Space Optics - ICSO 2018; 111800M. https://doi.org/10.1117/12.2535941.

Stein, A. F., Draxler, R. R, Rolph, G. D., Stunder, B. J. B., Cohen, M. D., Ngan, F., 2015. NOAA's HYSPLIT atmospheric transport and dispersion modeling system, *Bull. Amer. Meteor. Soc.*, *96*, 2059-2077. http://dx.doi.org/10.1175/BAMS-D-14-00110.

Suto, H., Kataoka, F., Kikuchi, N., Knuteson, R. O., Butz, A., Haun, M., Buijs, H., Shiomi, K., Imai, H., Kuze, A., 2021. Thermal and near-infrared sensor for carbon observation Fourier-transform spectrometer-2 (TANSO-FTS-2) on the Greenhouse Gases Observing Satellite-2 (GOSAT-2) during its first year on orbit, *Atmos. Meas. Tech., 14*, 2013–2039. https://doi.org/10.5194/amt-14-2013-2021.

Takagi, H., Saeki, T., Oda, T., Saito, M., Valsala, V., Belikov, D., Saito, R., Yoshida, Y., Morino, I., Uchino, O., Andres, R. J., Yokota, T., Maksyutov, S., 2011. On the benefit of GOSAT observations to the estimation of regional CO_2 fluxes, *SOLA*, *7*, 161-164. https://doi.org/10.2151/sola.2011-041.

Tanaka, T., Yates, E., Iraci, L., Johnson, M. S., Gore, W., Tadic, J.M., Loewenstein, M., Kuze, A., Frankenberg, C., Butz, A., Yoshida, Y., 2016. Two year comparison of airborne measurements of CO_2 and CH_4 with GOSAT at Railroad Valley, Nevada. *IEEE Trans. Geosci. Remote Sens. 54*, 4367–4375. https://doi.org/10.1109/TGRS.2016.2539973.

Turner, A. J., Jacob, D. J., Wecht, K. J., Maasakkers, J. D., Lundgren, E., Andrews, A. E., Biraud, S. C., Boesch, H., Bowman, K. W., Deutscher, N. M., Dubey, M. K., Griffith, D. W. T., Hase, F., Kuze, A., Notholt, J., Ohyama, H., Parker, R., Payne, V. H., Sussmann, R., Sweeney, C., Velazco, V. A., Warneke, T., Wennberg, P. O., Wunch, D., 2015. Estimating global and North American methane emissions with high spatial resolution using GOSAT satellite data, *Atmos. Chem. Phys.*, *15*, 7049–7069, https://doi.org/10.5194/acp-15-7049-2015.

Umezawa, T., Matsueda, H., Oda, T. Higuchi, K., Sawa, Y., Machida, T., Niwa Y., Maksyutov, S., 2020 Statistical characterization of urban CO_2 emission signals observed by commercial airliner measurements. *Sci. Rep., 10*, 7963, https://doi.org/10.1038/s41598-020-64769-9.

United Nations Environment Programme, The Montreal Protocol on Substances that Deplete the Ozone Layer, 14th Edition, 2020. ISBN: 978-9966-076-79-3.

United Nations Human Settlements Programme (UN-Habitat), 2012, Hot Cities: battle-ground for climate change, https://unhabitat.org/sites/default/files/2012/06/P1HotCities.pdf.

Varon, D. J., Jacob, D. J., McKeever, J., Jervis, D., Durak, B. O. A., Xia, Y., Huang, Y., 2018. Quantifying methane point sources from fine-scale satellite observations of atmospheric methane plumes, 2018. *Atmos. Meas. Tech*., *11*, 5673–5686, https://doi.org/10.5194/amt-11-5673-2018.

Veefkind, J. Aben, I., McMullan, K., Förster, H., de Vries, J., Otter, G., Claas, J., Eskes, H., de Haan, J., Kleipool, van Weele, M., Hasekamp, O., Hoogeveen, R., Landgraf, J., Snel, R., Tol, P., Ingmannc, P., Voors, R., Kruizinga, B., Vink, R., Visser, H., Levelt., P. F., 2012. TROPOMI on the ESA Sentinel-5 precursor: A GMES mission for global observations of the atmospheric composition for climate, air quality and ozone layer applications, the Sentinel missions—new opportunities for science, 2012. *Remote Sens. Environ.*, *120*, 70–83, https://doi.org/10.1016/j.rse.2011.09.027.

Verhulst, K. R., Karion, A., Kim, J., Salameh, P. K., Keeling, R. F., Newman, S., Miller, J., Sloop, C., Pongetti, T., Rao, P., Wong, C., Hopkins, F. M., Yadav, V., Weiss, R. F., Duren, R. M., Miller, C. E., 2017. Carbon dioxide and methane measurements from the Los Angeles Megacity Carbon Project – Part 1: calibration, urban enhancements, and uncertainty estimates, *Atmos. Chem. Phys.*, *17*, 8313–8341, https://doi.org/10.5194/acp-17-8313-2017.

Wang, Y., Ciais, P., Broquet, G., Bréon, F.-M., Oda, T., Lespinas, F., Meijer, Y., Loescher, A., Janssens-Maenhout, G., Zheng, B., Xu, H., Tao, S., Gurney, K. R., Roest, G., Santaren, D., Su, Y., 2019. A global map of emission clumps for future monitoring of fossil fuel CO_2 emissions from space, *Earth Syst. Sci. Data*, *11*, 687–703. https://doi.org/10.5194/essd-11-687-2019.

Wu, D., Lin, J. C., Fasoli, B., Oda, T., Ye, X., Lauvaux, T., Yang, E. G., Kort, E. A., 2018. A Lagrangian approach towards extracting signals of urban CO_2 emissions from satellite observations of atmospheric column CO_2 (XCO_2): X-Stochastic Time-Inverted Lagrangian Transport model ("X-STILT v1"), *Geosci. Model Dev.*, *11*, 4843-4871. https://doi.org/10.5194/gmd-11-4843-2018.

Wu, D., Lin, J. C., Oda, T., Kort, E.A., 2020. Space-based quantification of per capita CO_2 emissions from cities, *Environ. Res. Lett.*, 15, 035004. https://doi.org/10.1088/1748-9326/ab68eb.

Wunch, D., Toon, G. C., Blavier, J.-F. L., Washenfelder, R. A., Notholt, J., Connor, B. J., Griffith, D. W. T., Sherlock, V., and Wennberg, P. O., 2011. The Total Carbon Column Observing Network, *Phil. Trans. R. Soc. A*, 369, 2087–2112, https://doi.org/10.1098/rsta.2010.0240.

Xueref-Remy, I., Dieudonné, E., Vuillemin, C., Lopez, M., Lac, C., Schmidt, M., Delmotte, M., Chevallier, F., Ravetta, F., Perrussel, O., Ciais, P., Bréon, F.-M., Broquet, G., Ramonet, M., Spain, T. G., Ampe, C., 2018. Diurnal, synoptic and seasonal variability of atmospheric CO_2 in the Paris megacity area, *Atmos. Chem. Phys.*, *18*, 3335–3362, https://doi.org/10.5194/acp-18-3335-2018.

Yang, E. G., Kort, E. A., Wu, D., Lin, J. C., Oda, T., Ye, X., Lauvaux, L., 2020. Using space-based observations and Lagrangian modeling to evaluate urban carbon dioxide emissions in the Middle East, *J. Geophy. Res. Atmos.* https://doi.org/10.1029/2019JD031922.

Ye, X., Lauvaux, L., Kort, E.A., Oda, T., Feng, S., Lin, J.C., Yang, E.G., Wu, D., 2020. Constraining fossil fuel CO_2 emissions from urban area using OCO-2 observations of total column CO_2, *J. Geophy. Res. Atmos.* https://doi.org/10.1029/2019JD030528.

Yoshida, Y., Kikuchi, N., Morino, I., Uchino, O., Oshchepkov, S., Bril, A. Saeki T., Schutgens, N., Toon, G.C. Wunch, D.M. Roehl, C. M., Wennberg, P. O., Griffith, D. W. T., Deutscher, N. M., Warneke, T., Notholt, J., Robinson, J., Sherlock, V., Connor, B., Rettinger, M., Sussmann, R., Ahonen, P., Heikkinen, P., Kyrö, E., Mendonca, J., Strong, K., Hase, F., Dohe, S., Yokota. T.,, 2013. Improvement of the retrieval algorithm for GOSAT SWIR XCO_2 and XCH_4 and their validation using TCCON data. *Atmos. Meas. Tech.*, 6, 1533–1547. https://doi.org/10.5194/amt-6-1533-2013.Figure captions.

Fig.1. Example of a typical target observation pattern such as Beijing by GOSAT pointing and simultaneous observation of solar reflected light over the surface and thermal emissions from the Earth's atmosphere.

Fig. 2. GOSAT target points (red crosses) and megacity areas in this study (highlighted). (a) Beijing, (b) New Delhi, (c) New York City, (d) Riyadh, (e) Shanghai, and (f) Tokyo. We used the 1 × 1 km^2 ODIAC inventory map.

Fig. 3. Spatial distributions of XCO_2^{LT} (circles) obtained from target observations in March 2019 for (a) Beijing, (b) New Delhi, (c) New York City, (d) Riyadh, (e) Shanghai, and (f) Tokyo.

Fig. 4. XCO_2^{LT} enhancement plotted against the inverse of simulated wind speed from HYSPLIT using January‐March 2019 data with coefficient of determination (R^2) for (a) Beijing, (b) New Delhi, (c) New York City, (d) Riyadh, (e) Shanghai, and (f) Tokyo. Dashed lines and triangles show the linear fit and modeled background, respectively. The vertical lines show uncertainty for $XCO_2{}^{LT}{}_{aave}$ enhancement

Fig. 5. XCO_2^{LT} enhancement against the inverse of simulated wind speed from HYSPLIT using full-year 2019 data with coefficient of determination (R^2) for (a) Beijing, (b) Riyadh, and (c) Tokyo. The vertical lines show uncertainty for $XCO_2{}^{LT}{}_{aave}$ enhancement.

Fig. 6. XCO_2^{LT} enhancement against the inverse of simulated wind speed from HYSPLIT for Janunary‐March 2019 (circle and solid lines) and Jananuary‐March 2020 (diamonds and dotted lines) with coefficient of determination (R^2) for (a) Beijing (b) New Delhi (c) Riyadh, (d) New York (e) Shanghai, and (f) Tokyo. Triangles show the modeled background for individual megacities.

Fig. 7. CO_2 emission estimates of a city area from GOSAT against the city-wide ODIAC inventory estimates. Error bars show uncertainties in the emission estimate for an individual city by a least square regression. The calculated correlation coefficient (p) was 0.83.

Fig. A1. Flowchart of this study. Critical data are the GOSAT XCO_2^{LT} data products, wind speed from the HYSPLIT transport model, and the ODIAC inventory.

Fig. A2. CarbonTracker 2019B model at a local time of around 13:00 in February 2018 (left) and August 2018 (right) covering (a) Beijing, (b) New Delhi, (c) New York City, (d) Riyadh, (e) Shanghai, and (f) Tokyo.

Fig. A3. Impact of the inflow calculated by integrating the ODIAC inventory over the upwind area for (a) Beijing, (b) New Delhi, (c) New York City, (d) Riyadh, (e) Shanghai, and (f) Tokyo.

Fig. A4. Uncertainty model for XCO_2^{LT} enhancement. Uncertainty was assessed as a function of wind speed.

Tables

Table 1

Selected megacities and the number of cloud-free data collected with GOSAT between 2019 and 2020.

	Number of sampling points per city	the number of clear-sky datasets after screening cloud-contaminated data			Typical wind direction in winter at the time of GOSAT overpass
		winter 2019 (J-M)	2019 (J-D)	winter 2020 (J-M)	
Beijing	16	11	36	13	Northwest
New Delhi	16	6	N/A	7	Northwest
New York City	15	2	N/A	5	West
Riyadh	15*	11	34	12	West
Shanghai	13	3	N/A	1	Northwest
Tokyo	5	13	31	9	West

* Four before 2020.

Table 2

Coefficient $\alpha(i)$ from six megacities, their uncertainties, our estimated emissions using both winter months 2019 and 2020 data, emission estimates based on the ODIAC inventory, the inflow estimated from the intercept of relationship, and XCO_2^{LT} upwind by inflow based on the ODIAC inventory.

	$\alpha(i)$ (ppm m/s)	Uncertainty in $\alpha(i)$	Estimated emission (MtC/month/ city)	Integrated CO_2 emission inventory (ODIAC) (MtC/month/ city)	Estimated inflow (ppm) using Eq. A5	XCO_2^{LT} upwind by inflow (ppm) using Eq. A2
Beijing	21.1	50%	1.98	4.0	3.9	0.26
New Delhi	3.5	257%	0.33	2.2	2.1	0.33
New York City	8.8	155%	0.83	1.2	1.8	0.58
Riyadh	6.6	149%	0.62	2.2	2.2	0.09
Shanghai	19.8	120%	1.86	4.8	2.6	2.50
Tokyo	13.3	89%	1.25	2.7	1.7	0.78

Table 3

Coefficient $\alpha(i)$ from XCO_2^{LT} enhancement and NO_2 density differences between winter 2019 (January-March) and winter 2020 (January-March).

	$\alpha(i)$ (ppm m/s)		Changes	NO_2 (mol/m^{-2}) by TROPOMI		Changes
	Winter 2019	Winter 2020		Winter 2019	Winter 2020	
Beijing	28.5	19.9	-30%	2.4×10^{-4}	1.8×10^{-4}	-26%
New Delhi	3.8	3.3	-11%	1.6×10^{-4}	1.3×10^{-4}	-19%
New York City	50.0	8.6	-83%	1.6×10^{-4}	1.4×10^{-4}	-8%
Riyadh	16.3	4.4	-73%	1.1×10^{-4}	1.4×10^{-4}	+21%
Shanghai	20.9	18.2	-13%	2.4×10^{-4}	1.7×10^{-4}	-31%
Tokyo	16.5	10.8	-34%	1.5×10^{-4}	1.4×10^{-4}	-9%

1. Figures

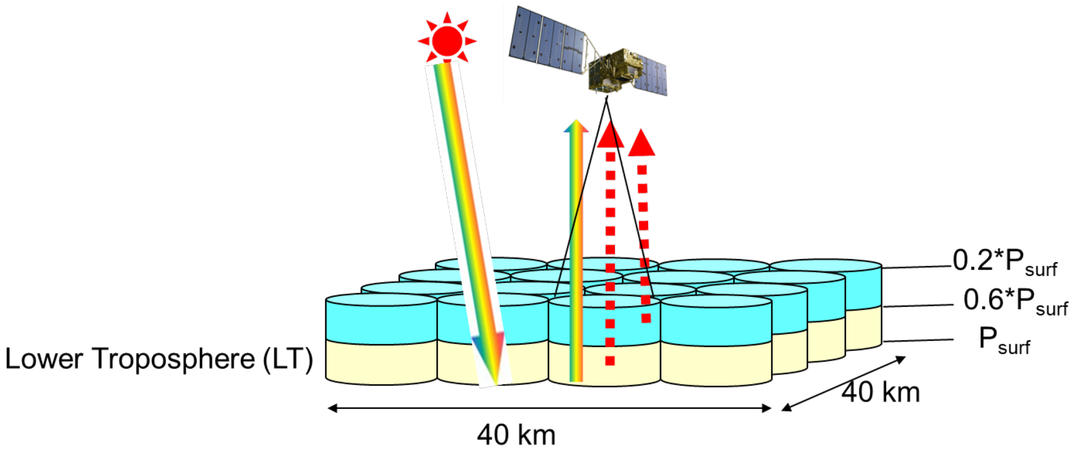

Fig. 1. Example of a typical target observation pattern such as Beijing by GOSAT pointing and simultaneous observation of solar reflected light over the surface and thermal emissions from the Earth's atmosphere.

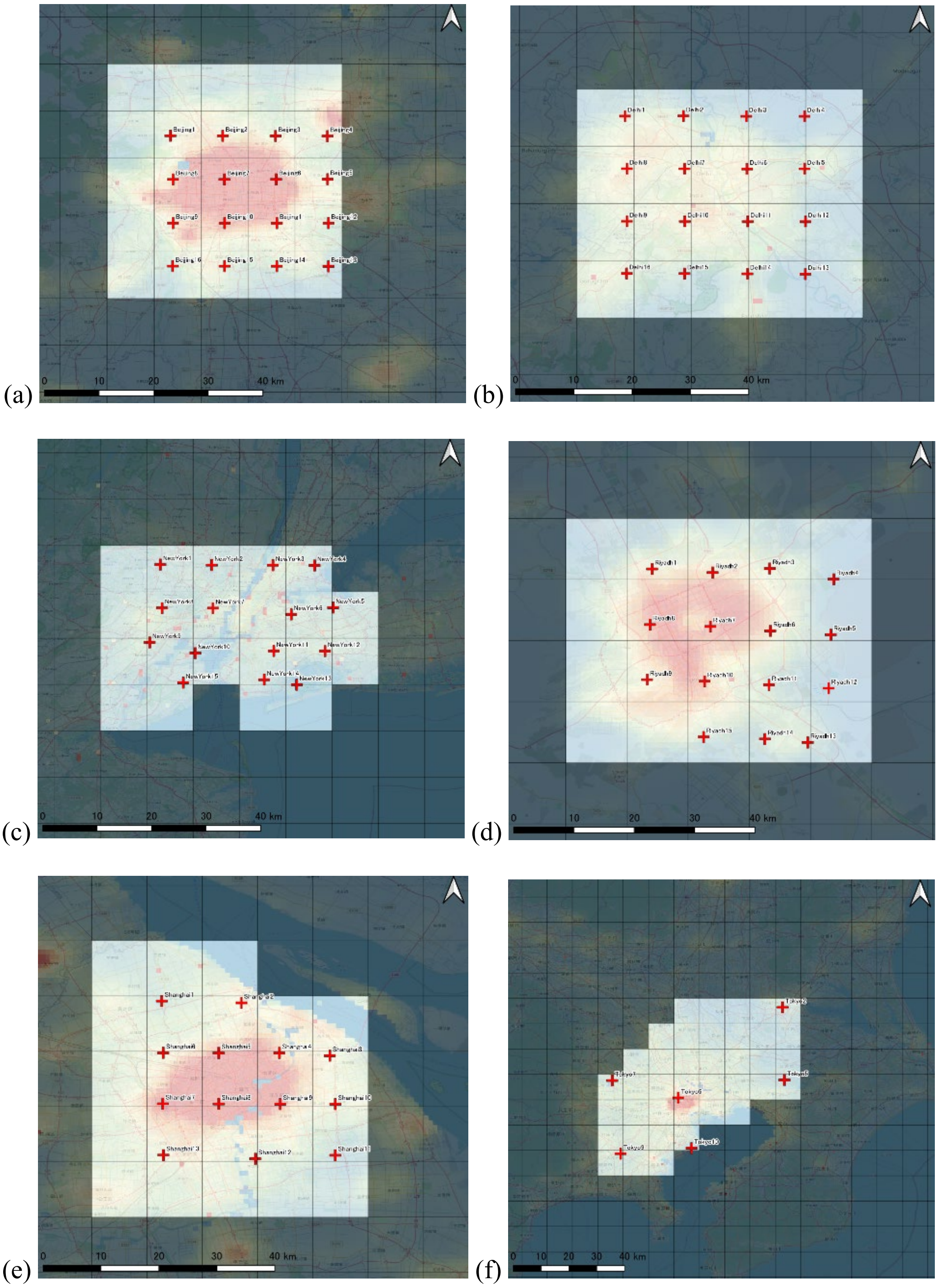

Fig. 2. GOSAT target points (red crosses) and megacity areas in this study (highlighted). (a) Beijing, (b) New Delhi, (c) New York City, (d) Riyadh, (e) Shanghai, and (f) Tokyo. We used the 1 × 1 km^2 ODIAC inventory map.

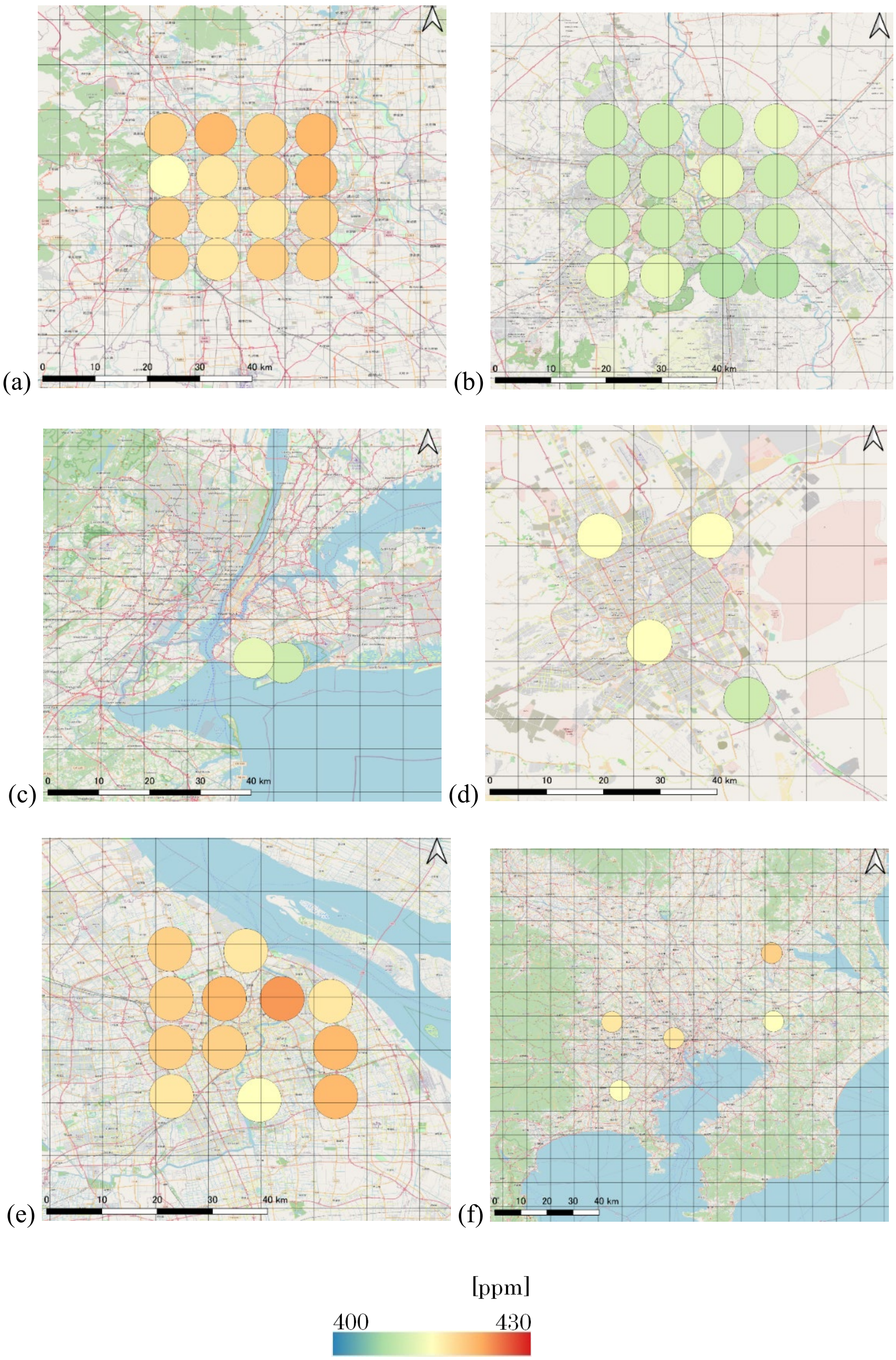

Fig. 3. Spatial distributions of XCO_2^{LT} (circles) obtained from target observations in March 2019 for (a) Beijing, (b) New Delhi, (c) New York City, (d)Riyadh, (e) Shanghai, and (f) Tokyo.

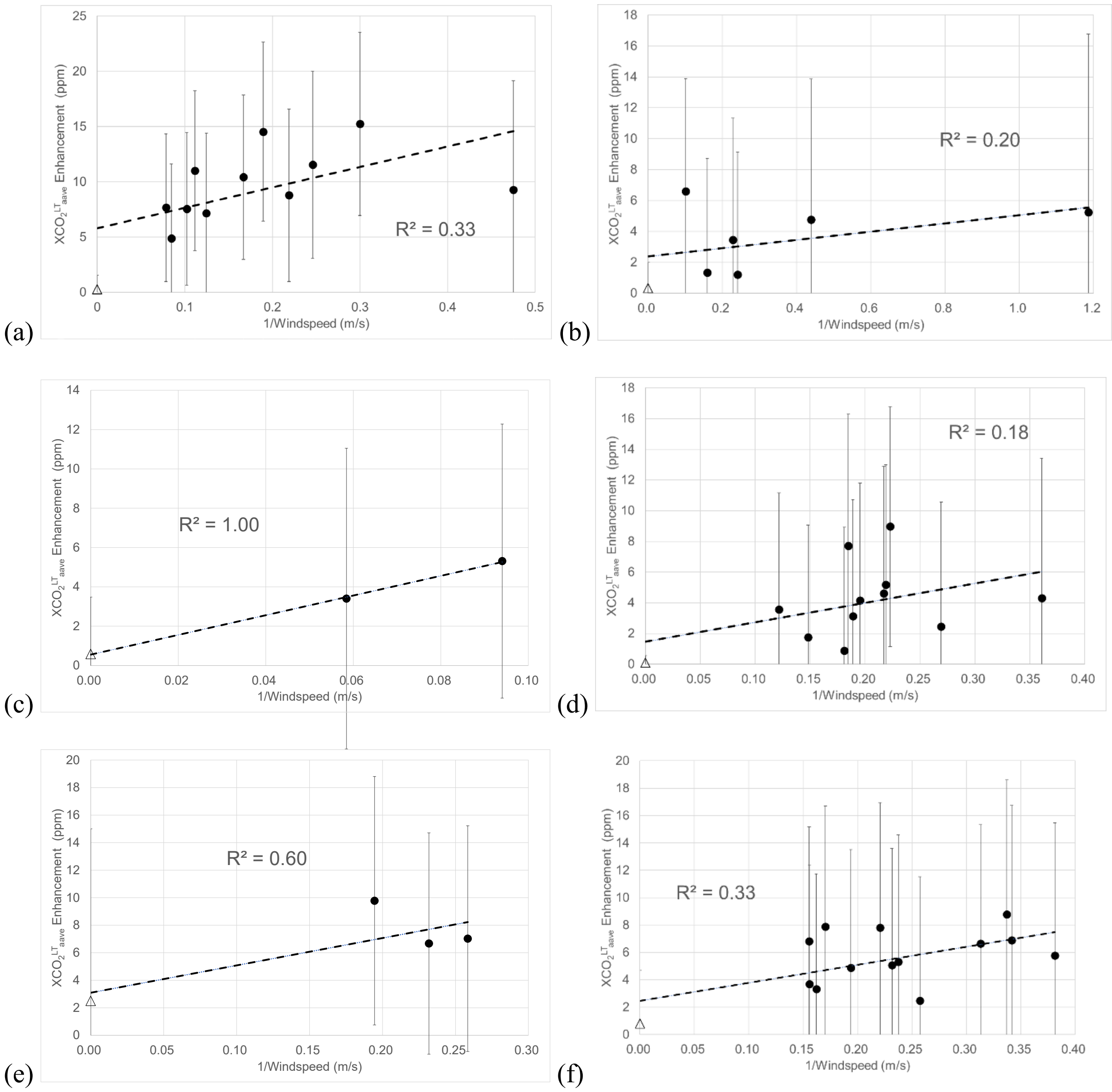

Fig. 4. XCO_2^{LT} enhancement plotted against the inverse of simulated wind speed from HYSPLIT using January-March 2019 data with coefficient of determination (R^2) for (a) Beijing, (b) New Delhi, (c) New York City, (d) Riyadh, (e) Shanghai, and (f) Tokyo. Dashed lines and triangles show the linear fit and modeled background, respectively. The vertical lines show uncertainty for $XCO_2^{LT}{}_{aave}$ enhancement.

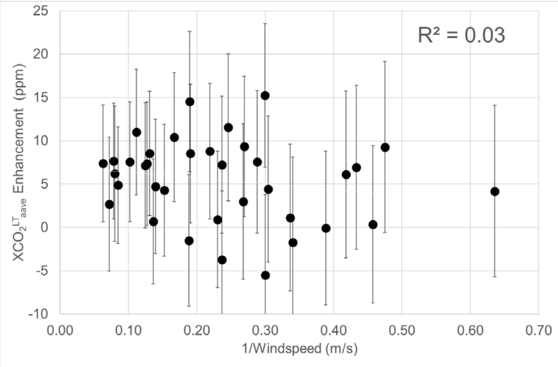

(a)

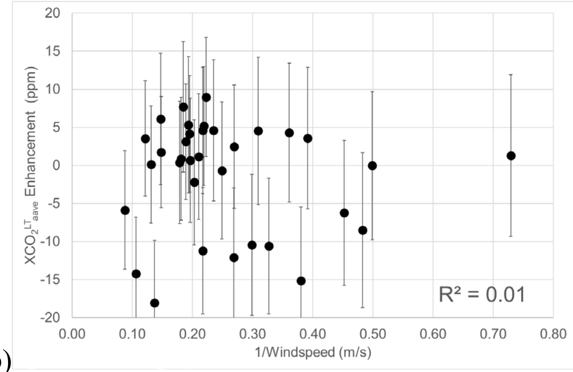

(b)

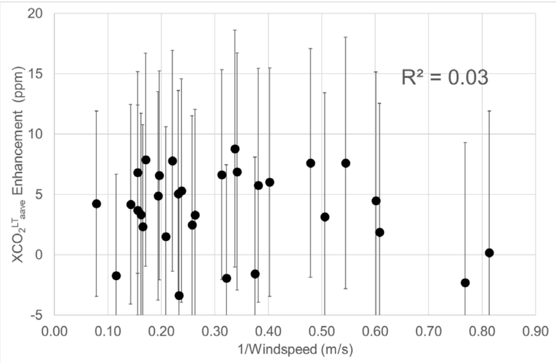

(c)

Fig. 5. XCO_2^{LT} enhancement against the inverse of simulated wind speed from HYSPLIT using full-year 2019 data with coefficient of determination (R^2) for (a) Beijing, (b) Riyadh, and (c) Tokyo. The vertical lines show uncertainty for $XCO_2^{LT}{}_{aave}$ enhancement.

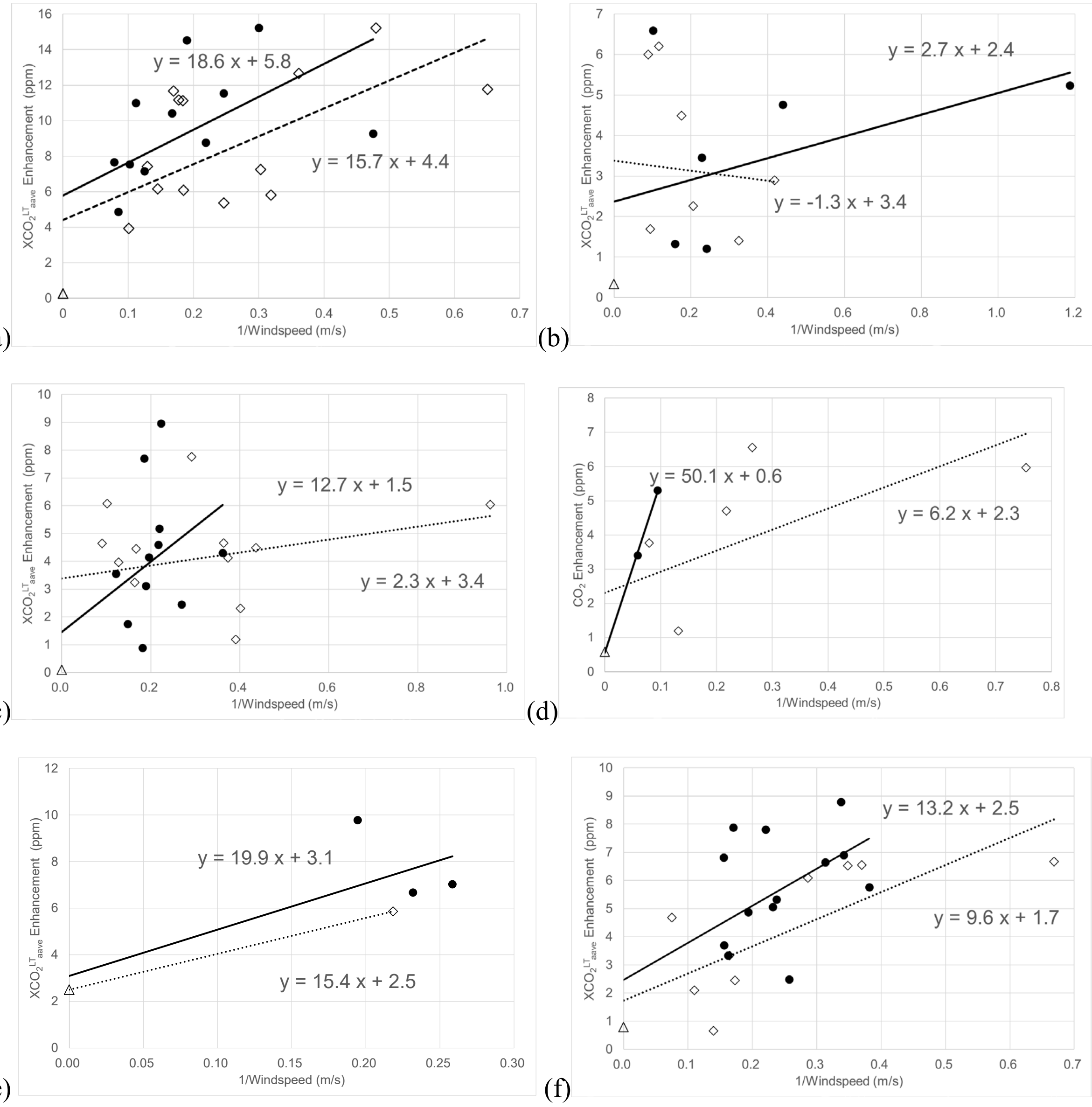

(a) (b)

(c) (d)

(e) (f)

Fig. 6. XCO_2^{LT} enhancement against the inverse of simulated wind speed from HYSPLIT for January–March 2019 (circle and solid lines) and January–March 2020 (diamonds and dotted lines) with coefficient of determination (R^2) for (a) Beijing (b) New Delhi (c) Riyadh, (d) New York (e) Shanghai, and (f) Tokyo. Triangles show the modeled background for individual megacities.

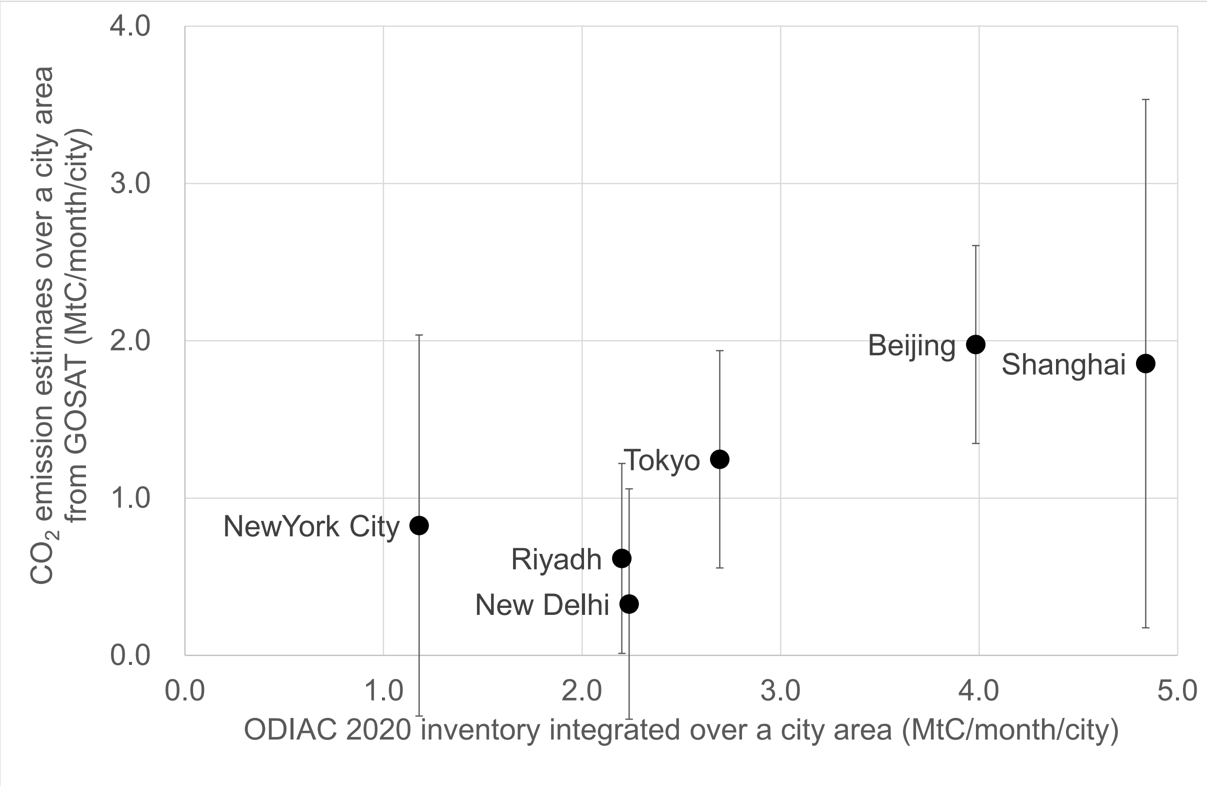

Fig. 7. CO_2 emission estimates of a city area from GOSAT against the city-wide ODIAC inventory estimates. Error bars show uncertainties in the emission estimate for an individual city by a least square regression. The calculated correlation coefficient (*p*) was 0.83.

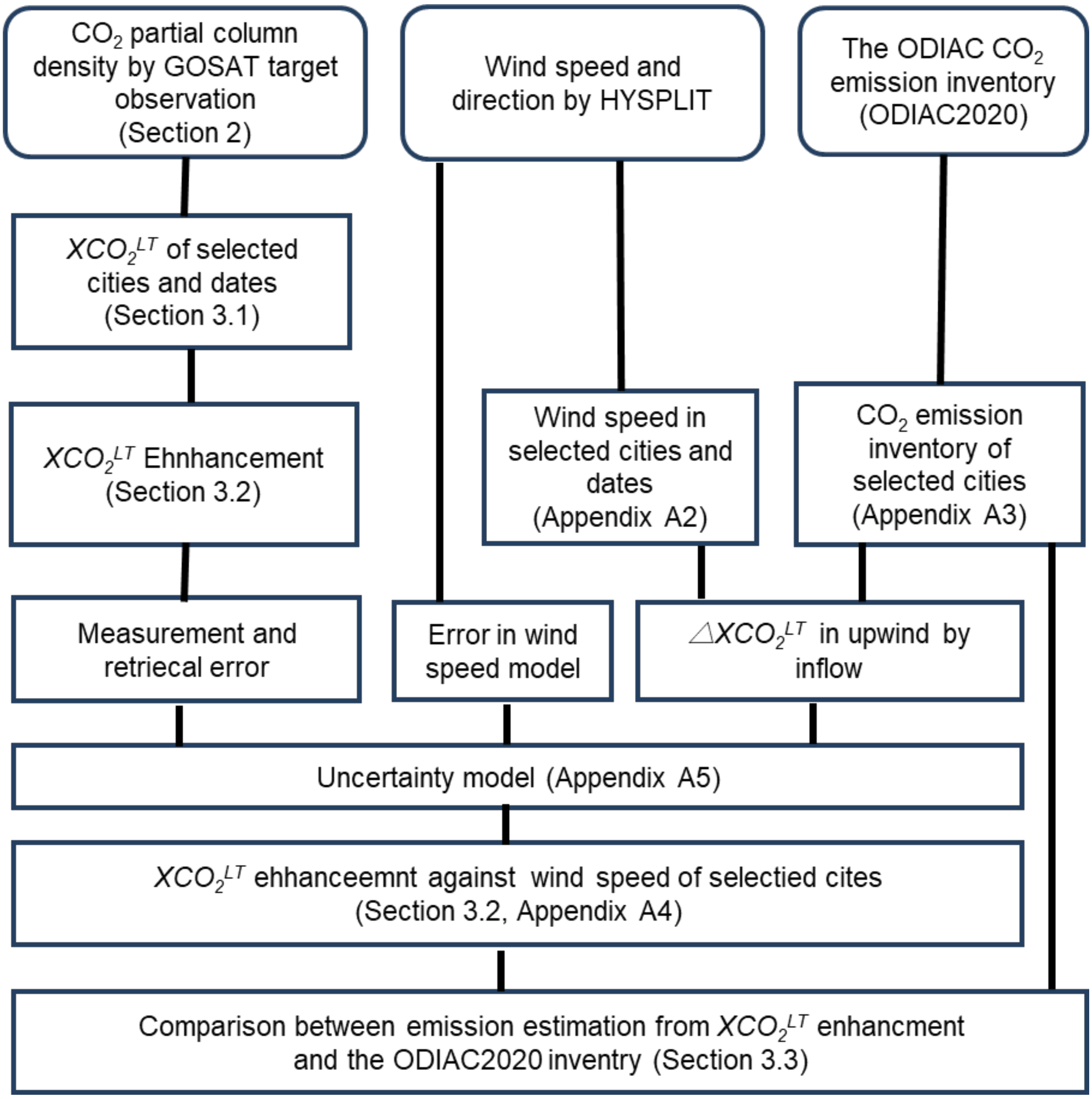

Fig. A1. Flowchart of this study. Critical data are the GOSAT XCO_2^{LT} data products, wind speed from the HYSPLIT transport model, and the ODIAC inventory.

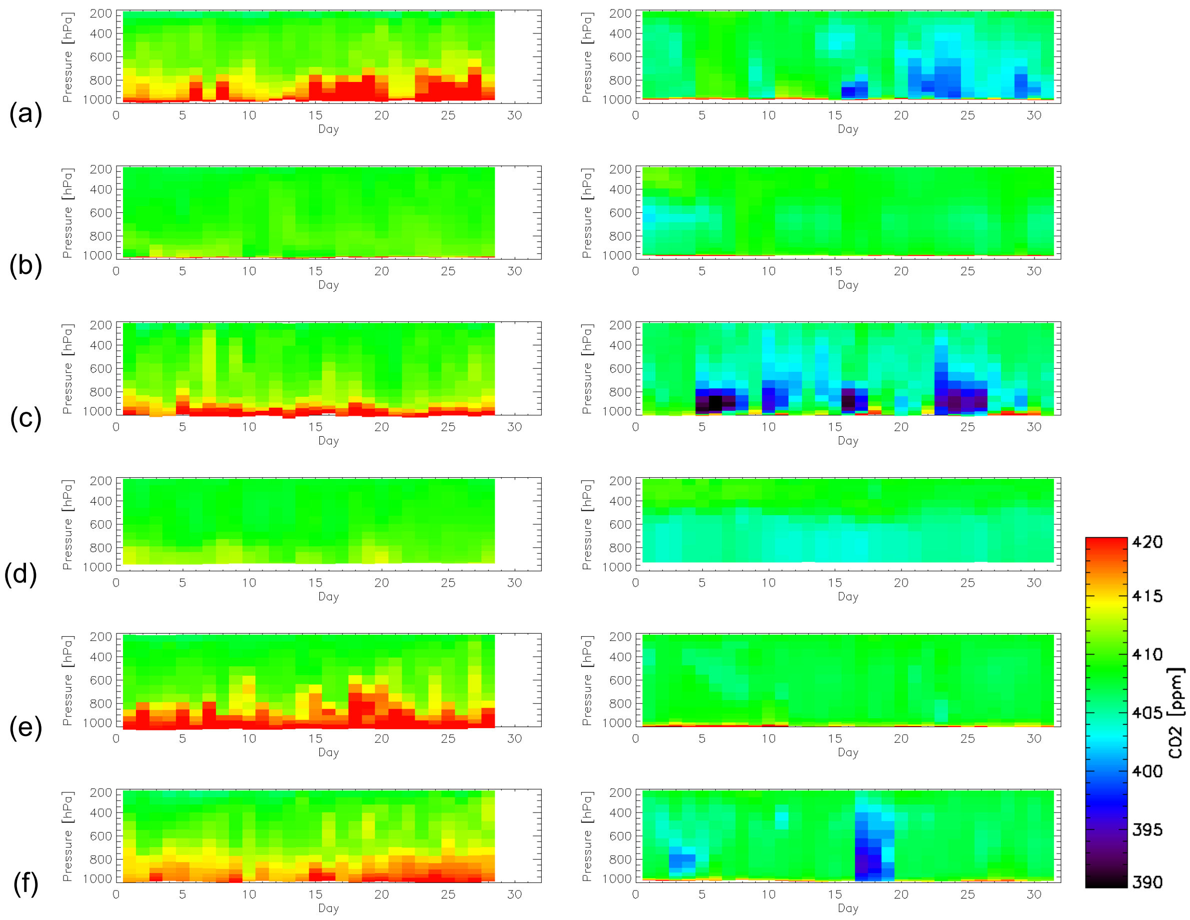

Fig. A2. CarbonTracker 2019B model at a local time of around 13:00 in February 2018 (left) and August 2018 (right) covering (a) Beijing, (b) New Delhi, (c) New York City, (d) Riyadh, (e) Shanghai, and (f) Tokyo.

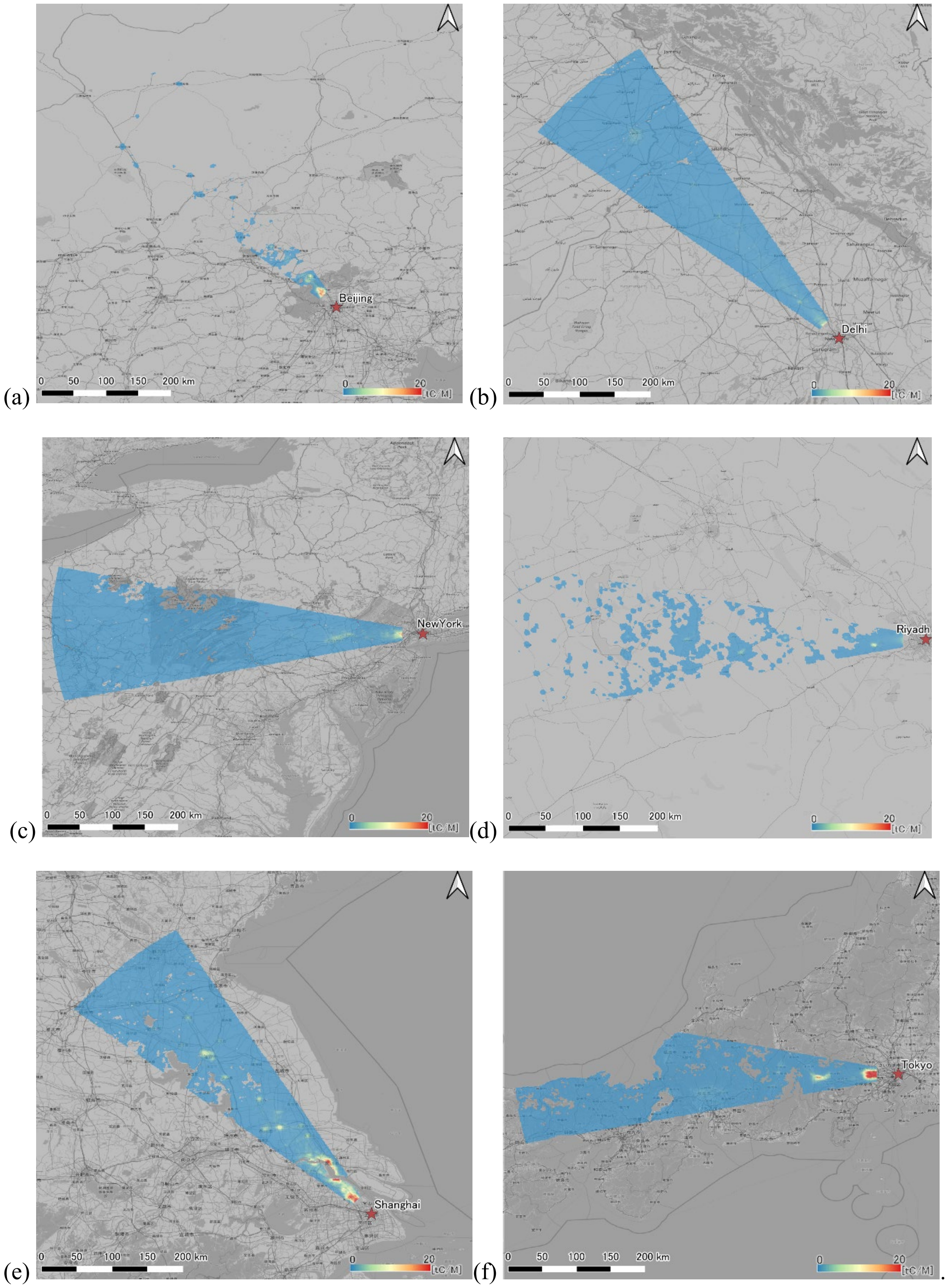

Fig. A3. Impact of the inflow calculated by integrating the ODIAC inventory over the upwind area for (a) Beijing, (b) New Delhi, (c) New York City, (d) Riyadh, (e) Shanghai, and (f) Tokyo.

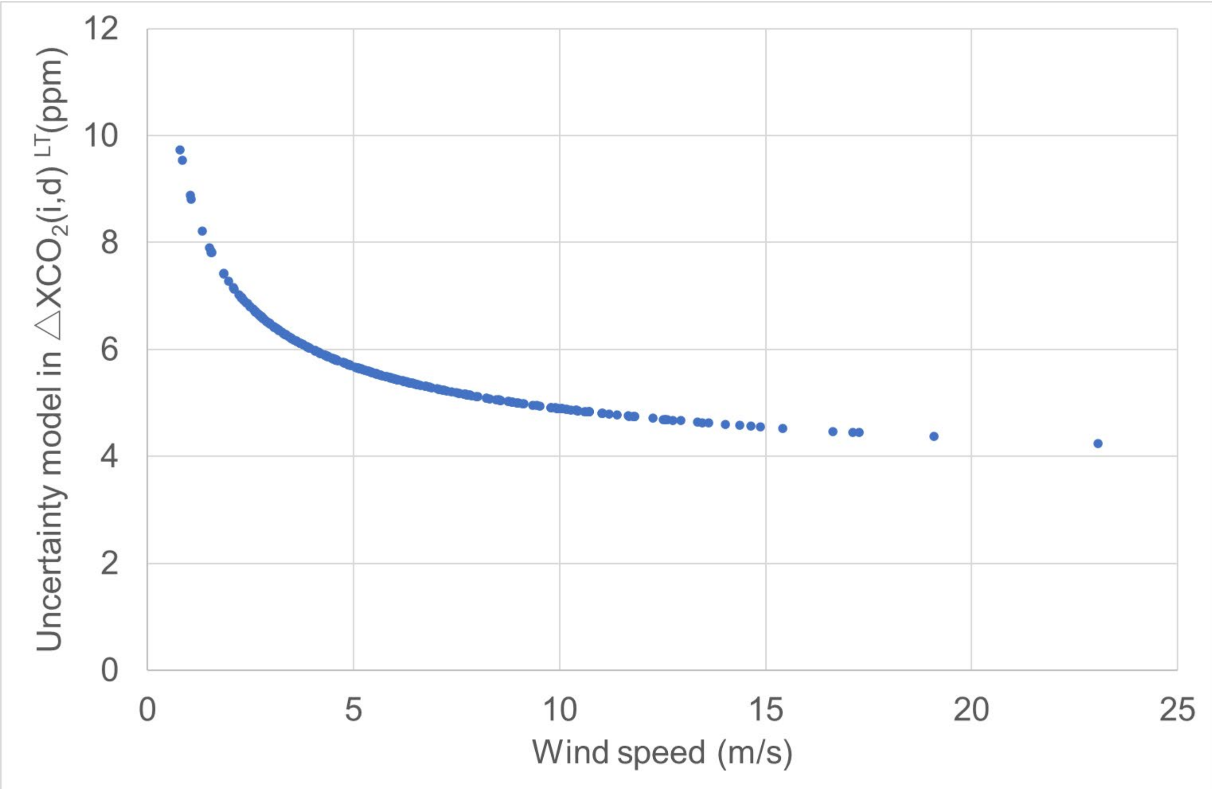

Fig. A4. Uncertainty model for XCO_2^{LT} enhancement. Uncertainty was assessed as a function of wind speed.